

ABSTRACT

Title of thesis: PATTERNED ACTIVE REGION MULTIMODE
 SWITCHES FOR OPTICAL THRESHOLDING:
 THEORY AND SIMULATION

Charles H. Camp Jr, Master of Science, 2005

Thesis directed by: Professor Julius Goldhar
 Department of Electrical and Computer Engineering

In modern telecommunications systems, glass fibers transport optical signals over thousands of kilometers with little loss or signal distortion. Although these fibers support a large bandwidth, the data rates are typically limited by the supporting electronics that produce, receive, and process the optical signals. To alleviate the demands placed upon the electronics, more processes can be done electro-optically and all-optically. One of the most fundamental components needed for such work is the optical switch or thresholder.

In this thesis a numerical model is built from basic electromagnetic theories in order to simulate the abilities of patterned active region multimode switches (PARMS) for use in optical thresholding. PARMS are active waveguide devices, which contain any number of electrically isolated active regions that can be independently biased for gain or loss. The simulation of one PARMS geometry is presented in this work, which demonstrates thresholding with a 23dB extinction ratio over a 6dB input power span.

PATTERNED ACTIVE REGION MULTIMODE SWITCHES
FOR OPTICAL THRESHOLDING:
THEORY AND SIMULATION

by

Charles H. Camp Jr

Thesis submitted to the Faculty of the Graduate School of the
University of Maryland, College Park in partial fulfillment
of the requirements for the degree of
Master of Science
2005

Advisory Committee:

Professor Julius Goldhar, Chair
Dr. Christopher Richardson
Professor Thomas Murphy

© Copyright by
Charles H. Camp Jr
2005

This is dedicated to my parents, advisors, and friends.

Mom and Dad - Thank you for the years of support and love.

Dr. Julius Goldhar - I don't even know where to begin: you took a naive and arrogant (I like to call it "confident") undergraduate and gave me a chance to thrive under your tutelage. I can only hope to make you proud as I take the next steps in my career. I will miss your stories, but hopefully I will be able to come to visit you and bring my own.

Dr. Chris Richardson - I cannot express my gratitude for the years of counsel you have selflessly (and patiently) given me.

Shuo-Yen Tseng - Thank you for all the help you provided me in my transition to graduate life and with my thesis. I hope our paths cross again.

The rest of my fellow graduate students - I can only hope that I have had a positive impact on your lives and maybe given you a few chuckles in recounting my "adventures".

All my friends - Just the other day we were crazy teenagers and now we are adults. I will cherish the times we have had. Each and every one of you helped me become the confident, happy person I am today – truly going beyond the call of duty. I will never be able to repay you all, but I will always try. We have been through a lot together.

TABLE OF CONTENTS

List of Figures	v
1 Introduction	1
2 Theory: Classic Electromagnetic Field Propagation Through Planar Dielectric Guides	6
2.1 Waveguide Modes	6
2.1.1 Guided Modes	6
2.1.2 Radiative Modes	14
2.2 Multimode Interference (MMI) Device Properties	15
3 Theory: Active Area Waveguides	19
3.1 Overview	19
3.2 Amplitude Effects: Saturable Gain and Absorption	19
3.3 Phase Effects in Saturable, Active Media	23
4 Numerics	25
4.1 Overview of Numerical Techniques	25
4.2 Modal Propagation Analysis (MPA)	27
4.2.1 The Effective Index Method	27
4.2.2 Modal Solutions	30
4.2.3 Modal Propagation Analysis	37
4.3 Modal Analysis with Radiative Modes	39
4.3.1 Radiative Modes	39
4.3.2 Reducing Simulation Window Reflections via the Virtual Boundary Condition (VBC)	44
4.4 Modal Propagation Analysis with Nonlinearities Incorporated	47
5 Patterned Active Region Multimode Switches (PARMS)	53
5.1 3-segment PARMS	53

6	Conclusion and Future Work	60
A	MATLAB Code: Solve for Guided Modes	63
B	MATLAB Code: Solve for Radiative Modes	74
C	MATLAB: Dual-Waveguide Mode Solutions	83
D	MATLAB: Modal Propagation Analysis of Guided Modes through Dual-Waveguides	93
E	MATLAB Code: Modal Propagation Analysis (MPA) with Radiative Modes and Patterned Active Regions	100
	Bibliography	119

LIST OF FIGURES

1.1	The ideal, step transfer function of an optical thresholder. In this case, the output power is held at the “low” state value regardless of the input power (below threshold), and the output power is clamped to the “high” state value if the input power is above threshold– regardless of how far above threshold.	3
1.2	The non-ideal thresholder has an input power span greater than zero and the output power ceases to maintain a constant value when the input power falls outside of a thresholding operational power range.	3
1.3	Simulation of a 30dB saturable absorber (SA). The SA’s gain function (left) is step-like with respect to input power, which results in an output power curve (right) that has no definite “high” or “low” state.	4
2.1	Schematic of a Indium-Phosphide ridge waveguide with a multiple quantum well (MQW) layer.	7
2.2	Schematic of a symmetric planar waveguide and a propagating ray. A ray is guided if the angle, θ , is larger than the critical angle.	7
2.3	Utilizing the effective index method, a 3-dimensional structure (see figure 2.1) is approximated by a 2-dimensional structure. A TE polarized field is shown incident on the front-face of the waveguide, which has a core-width of ‘d’. The dashed lines indicate the structure continues ad infinitum.	9

2.4	Plots of the right-hand sides (dots) and the left hand sides of equation 2.15 (solid) and 2.16 (dashed). The modes shown are from a 50 μm wide waveguide with a core and cladding index of 3.285 and 3.2833 respectively. From this plot, the discrete, guided-mode β 's can be calculated and by graphical inspection, one can see that four symmetric and three antisymmetric guided modes will propagate.	13
2.5	Simulation of light propagating through a 10 μm wide, 2 mm long MMI. There is a mirrored image of the input at approximately .97mm and an exact image at 1.94mm.	16
3.1	Gain versus input intensity solved numerically in MATLAB for a 10dB SOA (left) and a 10dB saturable absorber (right).	22
4.1	Cross-section of an active-core waveguide structure, which will serve as the basic geometry for all waveguides presented and simulated in this work.	28
4.2	The effective index method approximates the layers of each segment of the waveguide by a single index of refraction. This device is divided into three regions and each is approximated separately.	28
4.3	To determine the effective index of the central section of the waveguide drawn in figure 4.1, the segment is analyzed separately. The effective index of this segment is determined by observing the continuity of fields across each layer and determining the longitudinal propagation constant of the lowest-order guided TM mode propagating through just this section of the waveguide.	30
4.4	Plots of the left-hand sides of equations 4.1 (solid) and 4.2 (dot-dash) and the right-hand sides, which are the same (dash).	31

4.5	The normalized electric field pattern of the fundamental mode of a $2\mu m$ waveguide. The dashed lines represent the core-cladding boundaries. . . .	34
4.6	The two symmetric (left) and asymmetric (right) normalized mode patterns for a $28\mu m$ wide waveguide. The solid curves represent the lowest order symmetric/asymmetric mode and the dashed represents the highest (second in this case) symmetric/asymmetric mode. The solid vertical bars show the location of the core-cladding boundaries.	35
4.7	Drawing of a multimode waveguide with a varying input waveguide location. The ideal mode-shapes of both waveguides are superimposed atop each section of the guide. The input waveguide is single-moded and the MMI has four mode: two symmetric and two asymmetric.	36
4.8	These traces show the fraction of input power coupled into guided modes versus input waveguide width. Three different input waveguide positions were simulated: centered (solid), halfway (dash) between the center and the edge of the MMI, a third away from the edge (diamonds), and flush with the edge of the MMI's core (circles).	37
4.9	MPA simulation of light propagating through a .76mm long $2\mu m$ wide input waveguide and then coupling into a 5.5mm long, $28\mu m$ wide MMI. This waveguide supports four guided modes and is "weakly" guiding. White bars have been superimposed on the image to denote the (approximate) boundary between the core and cladding regions of the multimode waveguide.	38

4.10	MPA simulation of light propagating through a .76mm long $2\mu\text{m}$ wide input waveguide and then coupling into a 5.5mm long, $28\mu\text{m}$ wide MMI. This waveguide has an index contrast of 1.7%, and supports twenty-two modes (eleven symmetric and asymmetric). White bars have been superimposed on the image to denote the (approximate) boundary between the core and cladding regions of the multimode waveguide. The figure on the right zooms in on the single-mode, multi-mode interface to demonstrate the diffraction of the beam.	39
4.11	The absolute percentage difference between the infinite-window and bound-window γ solutions for the symmetric (left) and asymmetric (right) modes. The solid-line plots are the lower-order modes and the dashed the higher.	41
4.12	Normalized field intensity profile before (solid) and after coupling into the multimode waveguide from the single-mode input. The field intensity from incorporating guiding modes is shown with a dashed line, and the profile including radiative modes are cross-hatches. The field intensity profile coupled into guided and radiative modes accounts for nearly 100% of the total incident power; thus, the cross-hatches lie directly on top of the incident beam profile.	42
4.13	MPA simulation of a $28\mu\text{m}$ waveguide with radiative modes included. The left-hand figure demonstrates this multimode waveguide with a $2\mu\text{m}$ input waveguide centered on the front-face. The right-hand simulation is excited via a $2\mu\text{m}$ input waveguide offset by $7\mu\text{m}$ from the center of the front-face. The <i>choppy</i> distortions are caused by the radiative modes' energy reflecting off of the boundary window, which was given an artificial Dirichlet condition.	43
4.14	With Dirichlet boundary conditions enforced on the simulation windows' boundaries, the radiative modes will reflect at the boundary. This figure shows the reflection of two different radiation modes (solid and dashed)	44

4.15	The rays demonstrate the propagation of one radiative mode if Dirichlet conditions were imposed on the simulation boundary window (dotted) or at a virtual boundary (solid). With VBC, the same radiative mode can be simulated without concern over numerical reflections.	46
4.16	The simulation of a $28\mu m$ multimode waveguide with a $2\mu m$ input waveguide offset by $7\mu m$. This simulation utilized a $750\mu m$ VBC so that over 350 radiative modes are supported and there are no numerical reflections at the simulation windows' boundaries.	48
4.17	The intensity difference in a 2mm (1D) 30dB SOA between solving equation 4.16 numerically with the gain function as equation 4.18, $I_{out}(Exact)$, and approximating the gain function as equation 4.19, $I_{out}(Approx.)$, as a function of step-size, Δz	49
4.18	The intensity difference in a 2mm (1D) 30dB SOA between solving equation 4.16 numerically with the gain function as equation 4.18, $I_{out}(Exact)$, and approximating the gain function, $I_{out}(Approx.)$, as a function of Δz . The iterative method (solid) produces two orders of magnitude improvement over approximating the gain function as equation 4.19 (dashed). . .	51
4.19	In a split-step method, light is linearly propagated one step, Δz , and then all nonlinear action (e.g. gain, loss, etc.) are performed in an infinitesimally small region. After each nonlinear step, the exact coupling of the fields into each eigenmode (guided and radiative) is re-determined via overlap integrals.	51
4.20	Simulation of a 20dB SOA below (left) and above (right) saturation. With intensities far below saturation, the gain was calculated to be 19.7dB. For intensities above saturation, the device's gain was approximately -.15dB; thus, some energy was lost due to radiation and coupling losses.	52

5.1	Schematic of a 3-segment PARMS with symmetric, single-mode output waveguides. These two waveguides, as simulated, are fabricated with the same process as the PARMS; thus, they are also weakly guiding, and are both offset from the center of the end-face by $7\mu m$ (from center-to-center).	54
5.2	Simulation of an incident beam from a $7\mu m$ -offset, $2\mu m$ input waveguide into a $28\mu m$ multimode waveguide. The incident power is much higher than the saturation power for the active regions; therefore, the light propagates as if the waveguide were passive.	55
5.3	Schematic of a 3-segment PARMS with dimensions and values assigned.	56
5.4	Simulation of the 3-segments PARMS shown in figure 5.4 for input intensities far below saturation. As shown, a portion of the total input power has switched over to the “bar” state at the output.	56
5.5	Gain versus input power for the bar (left) and cross (right) state output of the PARMS shown in figure 5.3.	57
5.6	Output versus input power for the bar (left) and cross (right) state output of the PARMS shown in figure 5.3.	57
5.7	Schematic of a 3-segment PARMS with dimensions and values assigned.	58
5.8	Output power from the two output waveguides of the PARMS shown in figure 5.8. The bar state output (left) and the cross state output (right) both demonstrate thresholding abilities.	59
5.9	Output power from the two output waveguides of the PARMS shown in figure 5.8, but with no linewidth enhancement (intensity-dependent phase-shift). The bar state output (left) and the cross state output (right) both demonstrate greatly reduced thresholding capabilities as compared with figure 5.8 in which the Henry- α factor is 5.	59

6.1	Schematic of a 3-segment PARMS device in fabrication. The light-gray segments are the metal contacts and the black and dark-gray areas are the active waveguides (the dark-gray segments are the active waveguide with a layer of metal overtop).	61
6.2	Schematic of an 8-segment PARMS device in fabrication. The light-gray segments are the metal contacts and the black and dark-gray areas are the active waveguides (the dark-gray segments are the active waveguide with a layer of metal overtop).	61

Chapter 1

Introduction

From Alexander Graham Bell's photophone to the modern transoceanic fiber backbones, the use of optics in information transport and processing has become a major part of a trillion dollar telecommunications industry. What could be argued as the largest contributor to optical communications is the advent of fiber optics. With over 40 million kilometers of fiber laid world-wide, optical information transmission is the preferred means of long haul transmission [1].

The use of light for information transport and processing comes with many practical advantages over traditional copper wires. The most notable advantages of fiber-optics over copper lines (or similar systems) are the bandwidth, transmission losses, and signal clarity [2]. Although modern copper systems frequently operate at rates of gigabits per second (e.g. the Gigabit Ethernet Standard is 1Gbit/s over one hundred meters) and researchers have demonstrated 8.3 Gigabits per second over ten meters [3], there exists a strong relationship between bit-rate and length-of-wire. This relation arises from the skin-depth and dispersion. Skin-depth causes higher frequency signals to experience larger resistances than lower-frequency signals [4] and dispersion prevents temporally placing signals too close to each other. Glass fibers, on the other hand, are not conductors and have relatively low dispersion; thus, fibers can demonstrate Terabits-per-second performance over hundreds of kilometers with minimal signal distortion [1, 2].

With such large bandwidth possibilities, the maximum data rates in most communication systems are resultant of the electrical limitations in the transmission, detection, and processing circuitry. Because of these limitations, there is a certain commercial desire to do more work electro-optically and all-optically. One of the most basic components needed for such operations is an optical switch or thresholder. Thresholders act as signal interpreters by transmitting a constant “low” output power if the input power is below a threshold value and transmitting a constant “high” output power if the input is above the threshold. The figures of merit for a thresholder are the extinction ratio and the input power span. The extinction ratio is the power difference (in a logarithmic scale) between the high and low states, and the input power span is the amount of input power necessary to completely transition from the low to high state. The ideal thresholder has a step transfer function (see figure 1.1), which has a large output extinction ratio and instantaneously transfer from one state to the other at a threshold input power i.e. the input power span is zero. Realistically, these devices do not instantly change states at the threshold and their thresholding capabilities breakdown outside an operational range of input power (see figure 1.2).

A saturable absorber (SA) is basic thresholding device that demonstrates a step-like transmission function (P_{out}/P_{in}) with respect to the input power (see figure 1.3). The step-like transmission function produces output power that never maintains a constant “low” or “high” power state value. Research has shown improved thresholding characteristics if a saturable absorber and semiconductor optical amplifier (SOA) are placed in series, which improves the operational power range,

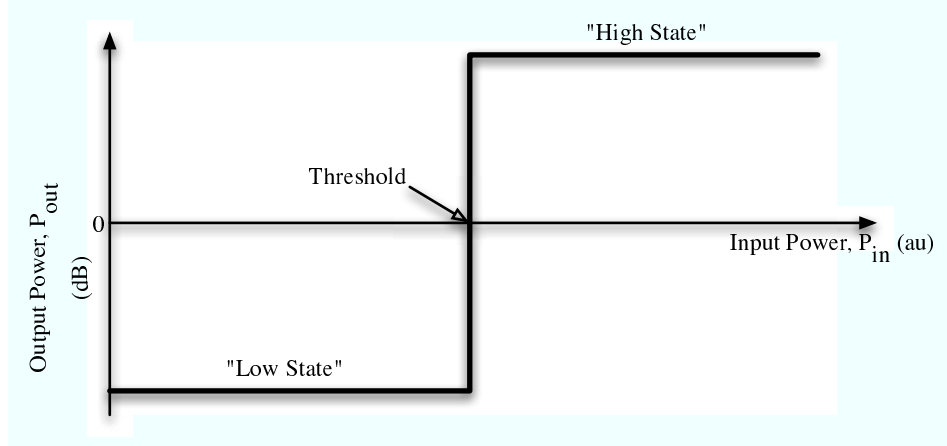


Figure 1.1: The ideal, step transfer function of an optical thresholder. In this case, the output power is held at the “low” state value regardless of the input power (below threshold), and the output power is clamped to the “high” state value if the input power is above threshold— regardless of how far above threshold.

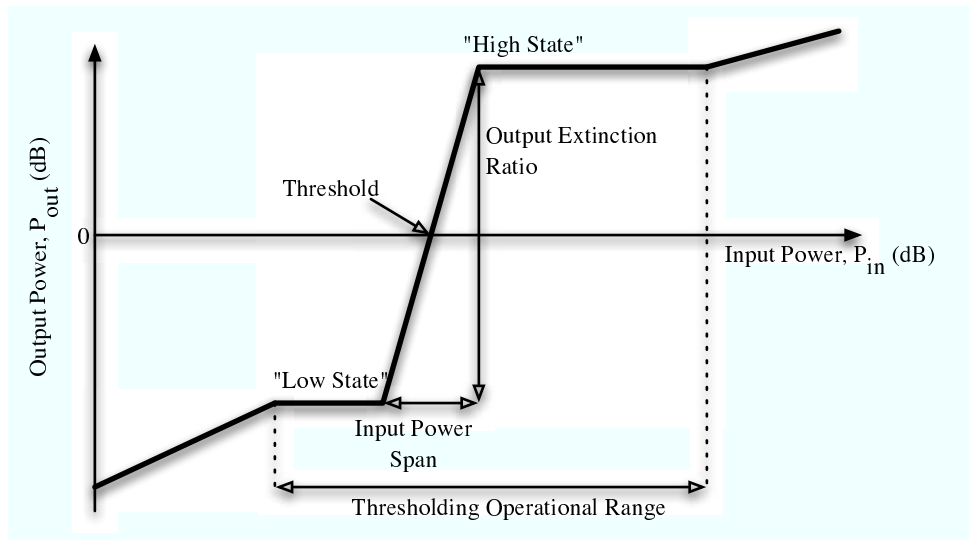


Figure 1.2: The non-ideal thresholder has an input power span greater than zero and the output power ceases to maintain a constant value when the input power falls outside of a thresholding operational power range.

the input power span, and the extinction ratio [5]. Performance is further improved by cascading these SA-SOA modules [6].

In addition to gain variations induced in these devices, there are also localized index variation. In single mode devices, these index modulations do not affect

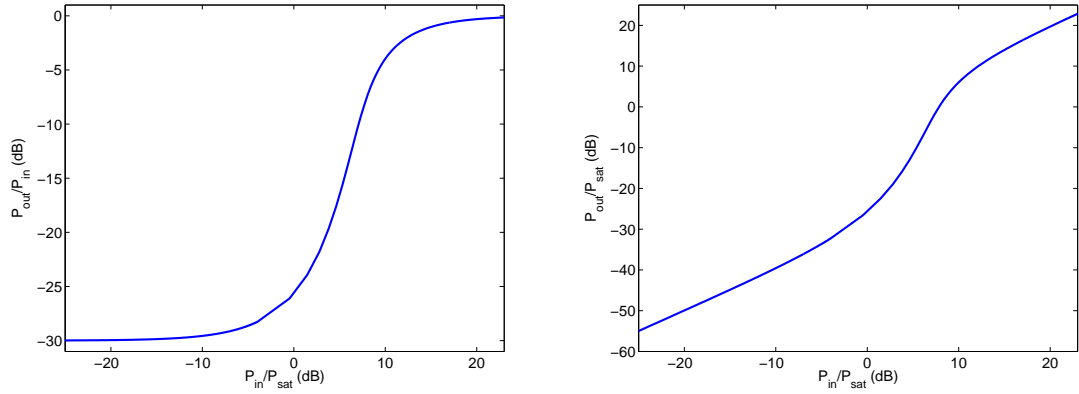


Figure 1.3: Simulation of a 30dB saturable absorber (SA). The SA’s gain function (left) is step-like with respect to input power, which results in an output power curve (right) that has no definite “high” or “low” state.

the thresholding characteristics, but in a multimode device they can dramatically alter the spatial distribution of power i.e. power switch. Multimode interference-semiconductor optical amplifiers (MMI-SOA) have demonstrated promising thresholding capabilities with large output extinction ratios over modest input power ranges [7, 8].

Although MMI-SOAs exploit active waveguide phase effects, these devices are still limited, like the single saturable absorber, by the homogeneity of the active region. In this thesis, multiple electrically isolated active regions within a single multimode waveguide are investigated. Chapter two reviews the fundamental concepts of linear electromagnetic field propagation through planar dielectric waveguides with special emphasis on radiative modes and the intrinsic imaging ability of multimode waveguides. Chapter three describes the amplitude and phase effects introduced by saturable gain/loss in active-area waveguides. With these devices falling outside of the ability of available computational tools, a numerical model was designed

as chapter four describes. The model was designed to handle realistic device designs including material and fabrication limitations. Chapter five demonstrates the simulation of a device and analyzes its thresholding characteristics.

Chapter 2

Theory: Classic Electromagnetic Field Propagation Through Planar Dielectric Guides

2.1 Waveguide Modes

2.1.1 Guided Modes

Dielectric waveguides transport light efficiently through the effect of total internal reflection (TIR). Because these waveguides operate via TIR, they are constructed from at least one core surrounded by materials with lower indices of refraction. A common example of a dielectric waveguide is a glass fiber, which is a dielectric waveguide with cylindrical symmetry about the core. The waveguides in this work are ridge waveguides of the form shown in figure 2.1. A ridge waveguide contains a single, rectangular core surrounded by one or more regions of lower indices of refraction.

Waves incident upon a symmetric ridge waveguide will either become confined within or decay out of the core into the other regions. Light that is confined within the waveguide resides in one or more guided “modes”, and the light that freely escapes the core of the waveguide is coupled to the radiative “modes”. In order for a ray to be confined within the core, the angle of incidence, θ , must be greater than the critical angle so that total internal reflection takes place i.e. $\theta \geq \sin^{-1}(n_{clad}/n_{core})$ (see figure 2.2). Each confined ray is a superposition of one or more guided “modes”,

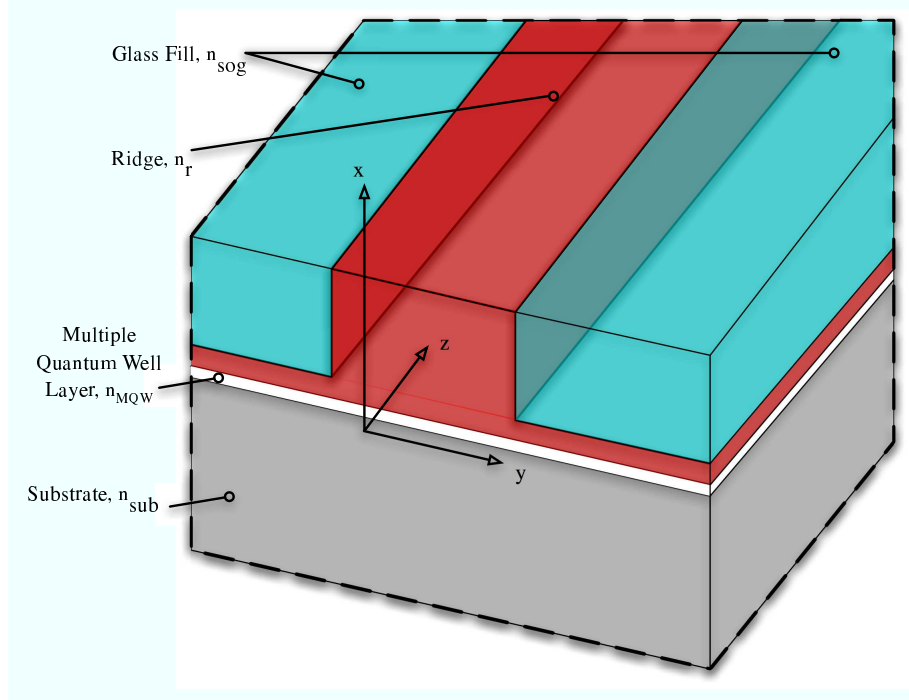


Figure 2.1: Schematic of a Indium-Phosphide ridge waveguide with a multiple quantum well (MQW) layer.

which are rays that follow TIR and their phase shifts by exactly 2π over one lateral round-trip. Although there is a continuum of angles with which rays can continually travel through the core, only a discrete set of angles meet the requirements of a guided mode [9, 10]. The continuum of angles, which do not meet the TIR condition, correspond to the infinite set of radiated modes.

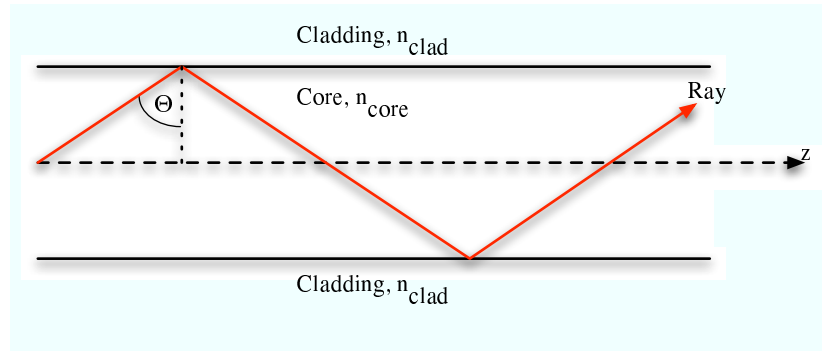


Figure 2.2: Schematic of a symmetric planar waveguide and a propagating ray. A ray is guided if the angle, θ , is larger than the critical angle.

In classic electromagnetic theory, fields are represented by the real-part of an exponential expression: $\Psi = Re\{\psi e^{j(\omega t - \beta z)}\}$, with ω being the carrier's radial frequency, ψ being the amplitude coefficient, and β being the longitudinal propagation constant. In this formalism, modes are described by their individual longitudinal propagation constants, β_ν , rather than their angle of propagation. As with any classical electromagnetic phenomena, modes can be described via Maxwell's equations:

$$\vec{\nabla} \times \vec{\mathcal{E}} = -\frac{\partial \vec{\mathcal{B}}}{\partial t} \quad (2.1)$$

$$\vec{\nabla} \times \vec{\mathcal{H}} = \vec{\mathcal{J}} + \frac{\partial \vec{\mathcal{D}}}{\partial t} \quad (2.2)$$

$$\vec{\nabla} \cdot \vec{\mathcal{D}} = \rho \quad (2.3)$$

$$\vec{\nabla} \cdot \vec{\mathcal{B}} = 0 \quad (2.4)$$

with $\vec{\mathcal{E}}$ and $\vec{\mathcal{H}}$ representing the electric and magnetic fields, respectively. $\vec{\mathcal{D}}$ and $\vec{\mathcal{B}}$ represent the electric and magnetic flux densities; while ρ is the charge density and $\vec{\mathcal{J}}$ is the current density. For mathematical simplicity, the effective index method is used to approximate the 3-dimensional waveguide by a 2-dimensional equivalent [11, 12]. The result of the effective index method is a planar waveguide such as shown in figure 2.3.

In working with a passive planar optical waveguide at low powers ($< 10mW$), a few assumptions may be made:

- (a) The material is non-magnetic (as most optical materials are not) i.e. $\mu = \mu_0$

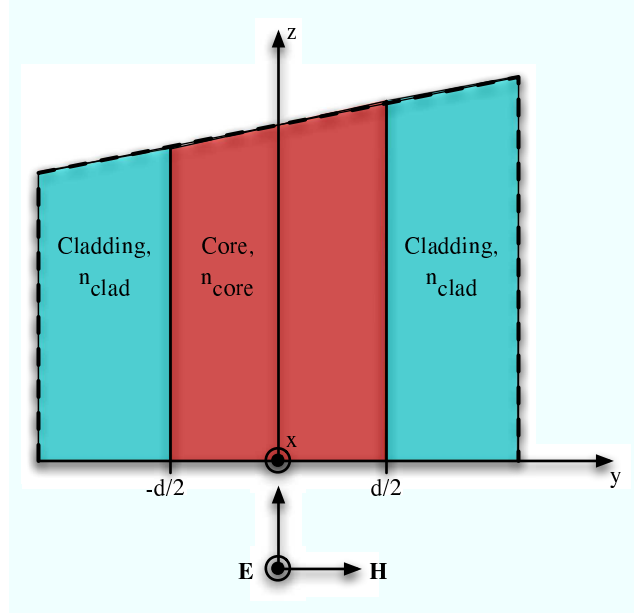


Figure 2.3: Utilizing the effective index method, a 3-dimensional structure (see figure 2.1) is approximated by a 2-dimensional structure. A TE polarized field is shown incident on the front-face of the waveguide, which has a core-width of 'd'. The dashed lines indicate the structure continues ad infinitum.

- (b) There is no free charge; ergo, there is neither current ($\vec{\mathcal{J}} = 0$), nor surface charge ($\rho = 0$)
- (c) Inside each region of the waveguide (e.g. core, cladding, etc.), the material is homogeneous and isotropic ($\vec{\epsilon} = \epsilon$)
- (d) Nonlinearities are negligible i.e. the susceptibility, $\chi = \chi^{(1)}$; therefore, $\vec{\mathcal{D}} = \epsilon \vec{\mathcal{E}}$
- (e) The fields are assumed to vary as the real part of $e^{j(\omega t - \beta z)}$ in time and longitudinal direction e.g. the electric field is

$$\vec{\mathcal{E}} = \text{Re}\{\vec{\mathbb{E}}(x, y)e^{j(\omega t - \beta z)}\} \quad (2.5)$$

- (f) Because this device is a guiding structure, the index of refraction must be

greater in the core than the adjacent regions.

Under these conditions, Maxwell's four equations can contract into Helmholtz's equation [10, 12]:

$$\nabla^2 \vec{\mathcal{E}} + \underbrace{\omega^2 \mu_0 \epsilon}_{\equiv k^2} \vec{\mathcal{E}} = 0, \quad (2.6)$$

which if the light is TE polarized ($\mathcal{E}_y = \mathcal{E}_z = \mathcal{H}_x = 0$), further reduces to

$$\partial_y^2 \vec{\mathcal{E}} + (k^2 - \beta^2) \vec{\mathcal{E}} = 0. \quad (2.7)$$

Equation 2.7 has a sinusoidal solution when $k^2 - \beta^2 > 0$ and an exponential solution when $k^2 - \beta^2 < 0$. Instead of describing the waveguide in figure 2.3 with one Helmholtz equation, three can be used: each equation describes the fields in one region of the waveguide, and electromagnetic boundary conditions couple each equation at the edge of their respective boundaries. For a symmetric planar waveguide, there are only two physical solutions: sinusoidal in the core and exponential in the cladding and sinusoidal in all regions. The former case corresponds to fields that are guided through the waveguide and the latter to radiated energy that is not confined. In equation 2.7 the fields are guided when $k_{cladding} \leq \beta \leq k_{core}$ and of the form [10]:

$$k^2 - \beta^2 = \begin{cases} \gamma^2 & \text{in the core} \\ -\alpha^2 & \text{in the cladding.} \end{cases} \quad (2.8)$$

$$\mathbb{E}_{gx}(y) = \begin{cases} Ae^{\alpha(y+\frac{d}{2})} + Be^{-\alpha(y+\frac{d}{2})} & \text{if } y \leq -\frac{d}{2} \\ D \cos(\gamma y) + F \sin(\gamma y) & \text{if } -\frac{d}{2} \leq y \leq \frac{d}{2} \\ Ge^{\alpha(y-\frac{d}{2})} + He^{-\alpha(y-\frac{d}{2})} & \text{if } y \geq \frac{d}{2}, \end{cases} \quad (2.9)$$

where A,B,D,F,G, and H are constants describing field amplitude and d is the core width. This equation may be split into two separate solutions: one with F = 0 and the other with D=0. These solutions represent the “symmetric” and “antisymmetric” (or “asymmetric”) modal solutions, respectively. With the two solutions separated, the total guided-field solution is the summation of the symmetric and asymmetric solutions.

Just as the ray-optics description of modes produced a discrete set of guided modes, so does the solution to equation 2.7 (in this case for TE polarized light). As previously mentioned, variables A,B,C,D,F,G, and H insure the field continuity across the boundary and the continuity of the fields’ derivatives. Additionally, guided mode fields decay to zero at an infinite lateral distance from the waveguide. For the symmetric, guided mode case F = 0, B = 0, and G = 0; therefore, equation 2.9 is re-written:

$$\mathbb{E}_{gx}^{Sym}(y) = \begin{cases} Ae^{\alpha(y+\frac{d}{2})} & \text{if } y \leq -\frac{d}{2} \\ D \cos(\gamma y) & \text{if } -\frac{d}{2} \leq y \leq \frac{d}{2} \\ He^{-\alpha(y-\frac{d}{2})} & \text{if } y \geq \frac{d}{2}. \end{cases} \quad (2.10)$$

Matching the boundary conditions,

$$A = D \cos(-\gamma \frac{d}{2}) \quad (2.11)$$

$$\alpha A = \gamma D \sin(\gamma \frac{d}{2}) \quad (2.12)$$

$$H = D \cos(\gamma \frac{d}{2}) \quad (2.13)$$

$$\alpha H = \gamma D \sin(\gamma \frac{d}{2}), \quad (2.14)$$

and combining the expressions produces

$$\tan(\gamma \frac{d}{2}) = \frac{\alpha}{\gamma}. \quad (2.15)$$

Following the same procedure for the antisymmetric case results in

$$-\cot(\gamma \frac{d}{2}) = \frac{\alpha}{\gamma}. \quad (2.16)$$

Equation 2.15 and 2.16 are transcendental equations; therefore, graphical or numerical techniques (e.g. the Newton-Raphson method [16]) are needed to solve for their solutions. Figure 2.4 displays the plots of the left and right-hand sides of equations 2.15 and 2.16 in terms of γ . The solutions are represented graphically in figure 2.4 as the points of intersection of the two curves.

Symmetric planar waveguides always support at least one guided mode; therefore, equation 2.15 will result in at least one solution, and equation 2.16 will produce exactly one fewer or as many solutions. Each solution corresponds to a mode and

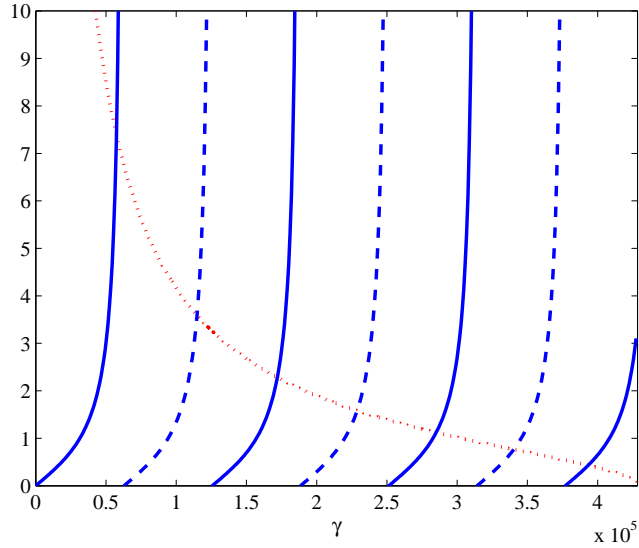


Figure 2.4: Plots of the right-hand sides (dots) and the left hand sides of equation 2.15 (solid) and 2.16 (dashed). The modes shown are from a $50 \mu\text{m}$ wide waveguide with a core and cladding index of 3.285 and 3.2833 respectively. From this plot, the discrete, guided-mode β 's can be calculated and by graphical inspection, one can see that four symmetric and three antisymmetric guided modes will propagate.

equation 2.10 is re-written as a series solution of the individual modes [10, 17]:

$$\mathbb{E}_{gx}^{Sym}(y) = \vec{a}_x \sum_i c_i \psi_i = \begin{cases} \sum_i A_i e^{\alpha_i(y + \frac{d}{2})} & \text{if } y \leq -\frac{d}{2} \\ \sum_i D_i \cos(\gamma_i y) & \text{if } -\frac{d}{2} \leq y \leq \frac{d}{2} \\ \sum_i H_i e^{-\alpha_i(y - \frac{d}{2})} & \text{if } y \geq \frac{d}{2}. \end{cases} \quad (2.17)$$

The mode vectors, $\vec{a}_x \psi_i$'s, for both the symmetric and asymmetric modes form an orthonormal set; thus in the symmetric case, for example, the amplitude coefficients (A_i , D_i , and H_i) not only ensure continuity at the boundary conditions, but also modal normality ($\int |\psi_i|^2 dy = 1$). The coefficient c_i (in equation 2.17) describes how much of the incident field is coupled into the i^{th} mode. This ‘‘coupling coefficient’’

is determined via an overlap integral:

$$c_i = \int \mathbb{E}_x(y) \psi_i^*(y) dy, \quad (2.18)$$

where $E_x(y)$ is the TE-polarized incident field and $\psi_i(y)$ is the normalized mode shape of the i^{th} mode.

2.1.2 Radiative Modes

Another physically realizable solution to equation 2.7 is that of radiative modes. As the name implies, the energy in these modes does not remain in the core. Mathematically, equation 2.7 will have sinusoidal solutions in all three segments of the waveguide when $0 \leq \beta \leq k_{clad}$; therefore,

$$k^2 - \beta^2 = \begin{cases} \gamma^2 & \text{in the core} \\ -\alpha^2 & \text{in the cladding.} \end{cases} \quad (2.19)$$

$$\mathbb{E}_{rx}(y) = \begin{cases} A \sin[\alpha(y + \frac{d}{2})] + B \cos[-\alpha(y + \frac{d}{2})] & \text{if } y \leq -\frac{d}{2} \\ D \sin(\gamma y) + F \cos(\gamma y) & \text{if } -\frac{d}{2} \leq y \leq \frac{d}{2} \\ G \sin[\alpha(y - \frac{d}{2})] + H \cos[-\alpha(y - \frac{d}{2})] & \text{if } y \geq \frac{d}{2}. \end{cases} \quad (2.20)$$

In the same manner as for the guided-mode solution, a set of expressions

describes the matching boundary conditions:

$$D \sin(\gamma \frac{d}{2}) = H \quad (2.21)$$

$$\gamma D \cos(\gamma \frac{d}{2}) = G\alpha \quad (2.22)$$

$$-D \sin(\gamma \frac{d}{2}) = B \quad (2.23)$$

$$\gamma D \cos(\gamma \frac{d}{2}) = \alpha A \quad (2.24)$$

for the asymmetric case. Unlike with guided-mode, these four equations do not condense to produce a transcendental equation with a discrete set of solutions. Even though there is an infinite number of solutions, they still form an orthogonal set— in fact, the combined set of solutions for the guided and radiative modes form a complete, orthogonal set of solutions to Helmholtz’s equation for this geometry (symmetric, planar waveguide) [10]. Additionally, radiative modes may only be discussed in the reference of a finite window; otherwise, energy is not conserved as they are sinusoidal ad infinitum. More on radiative mode windowing will be discussed in chapter 4.

2.2 Multimode Interference (MMI) Device Properties

Multimode Interference (MMI) devices, as the name suggests, allow the propagation of several modes. Multi-mode interference devices have conventionally acted as low-loss splitter/couplers [18]; although, they have also found use as optical flip-flops [19, 20] and modulators [17]. Most devices constructed from a multimode waveguide take advantage of the self-imaging property [17]: an input field propagating through

a multimode waveguide will produce a mirrored image of the input at a certain length (as shown in figure 2.5) and an exact image at twice this length (as well as more mirrored and exact images at integer multiples of these lengths).

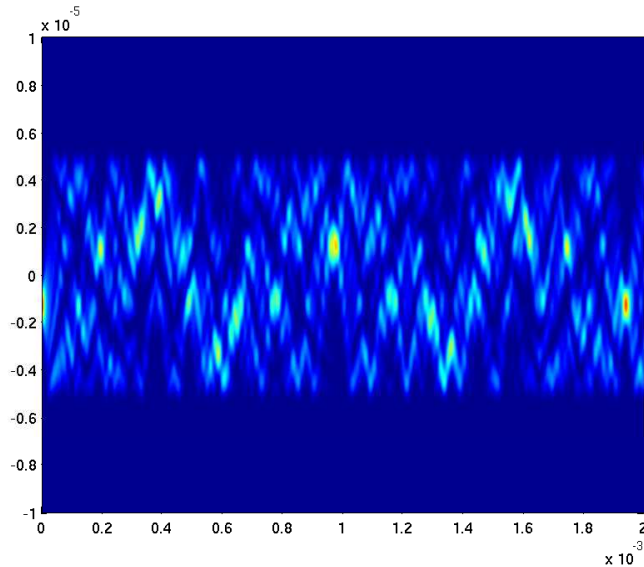


Figure 2.5: Simulation of light propagating through a $10 \mu m$ wide, 2 mm long MMI. There is a mirrored image of the input at approximately .97mm and an exact image at 1.94mm.

Self-imaging arises from beating between the modes. The beat length of the two lowest-order modes is:

$$L_\pi = \frac{\pi}{\beta_0 - \beta_1}, \quad (2.25)$$

which is often approximated as

$$L_\pi \approx \frac{4n_{core}W_e^2}{3\lambda_0}, \quad (2.26)$$

where W_e is the effective width of the waveguide, n_{core} is the core's index of refraction, and λ_0 is the propagating light's wavelength under vacuum. The effective width

accounts for the amount to which the fields of the guided modes penetrate into the cladding [21]. Under most circumstances, the effective width can be approximated by the effective width of the fundamental guided mode i.e.

$$W_e = d + \left(\frac{\lambda_0}{\pi}\right) \left(\frac{n_{clad}}{n_{core}}\right)^{2\sigma} \frac{1}{\sqrt{n_1^2 - n_2^2}}, \quad (2.27)$$

where d is the width of the waveguide's core and σ is a constant which equals 0 for TE polarized light and 1 for TM.

The exact imaging-length of the device (with respect to the beat-length) depends on the type of input excitation. “Symmetric interference”, for example, results from a center-fed multimode waveguide having only the even, symmetric modes excited [17]. The imaging length for a “symmetric interference” device is $3L_\pi/4$. For our devices, no restrictions are placed on the type of input excitation; thus, they are “general interference” devices. Devices operating under the “general interference mechanism” have an imaging length of $3L_\pi$, where a mirrored-image is produced (and an exact replica at twice this length). As the index contrast (difference in core and cladding indices of refraction) becomes smaller, the waveguide becomes “weakly guiding”, and the exact imaging lengths deviate from the aforementioned approximations. As will be seen in upcoming chapters, the imaging still occurs, but the exact image is *smear*ed out because the field penetration into the cladding becomes very different for each mode. The resolution of a multimode waveguide is approximately

$$\rho \approx \eta \frac{W_{em}}{m}, \quad (2.28)$$

where ρ is the resolution, η is a factor related to what type of guided mode spectra the waveguide contains (usually set to 1), W_{em} is the effective width of the highest-order guided mode, and m is the number of guided modes [17].

Besides imaging properties, multimode waveguides also have relaxed fabrication tolerances, large bandwidth operation, and low-loss input- and output-coupling [17, 22]; which has led to further enthusiasm over their use in integrated systems.

Chapter 3

Theory: Active Area Waveguides

3.1 Overview

Passive waveguides, as described in the previous chapter, provide a medium with no additional sources of energy by which light can propagate. Active waveguides, on the other-hand, do include an external energy source, which affects the linear and nonlinear response of the system to the incident fields. “Opto-electronic” devices, for example, in which free carriers are externally injected into the waveguide, can produce large nonlinear effects even at low incident beam intensities, and have resulted in devices such as the semiconductor optical amplifier (SOA) and integrated Mach-Zehnder interferometers (MZI).

In the remainder of this chapter, the amplitude and phase effects resulting from an active semiconductor waveguide will be briefly reviewed.

3.2 Amplitude Effects: Saturable Gain and Absorption

To simplify the simulation of an absorber or amplifier, a semiconductor waveguide is approximated by a collection of non-interacting two-level systems:

$$\frac{\partial N}{\partial t} = \frac{i}{qV} - \frac{N}{\tau_c} - \frac{g(N)}{\hbar\omega} I, \quad (3.1)$$

in which i is the injection current, V is the volume of the active region, N is the carrier concentration, τ_c is the spontaneous carrier lifetime, $g(N)$ is the differential gain, and I is the incident beam intensity [23]. In this equation, the differential gain is defined as

$$g(N) = \sigma(N - N_0) \quad (3.2)$$

in which N_0 is the carrier density at transparency and σ is the absorption cross-section. From these two expressions, the time-dependent relationship between differential gain (g) and its unsaturated value (g_0), spontaneous carrier lifetime (τ_c), beam power (P), and saturation energy (E_{sat}) is formed:

$$\frac{\partial g}{\partial t} = \frac{g - g_0}{\tau_c} - \frac{gP}{E_{sat}}. \quad (3.3)$$

In steady-state this equation simplifies to

$$g = \frac{g_0}{1 + \frac{I}{I_{sat}}} \quad (3.4)$$

where $I_{sat} = E_{sat}/A\tau_c$ is the saturation intensity and A is the cross-sectional area of the active region.

The equation describing the evolution of beam intensity in space is formed from an augmented version of the Helmholtz equation:

$$\nabla^2 \vec{\mathcal{E}} + k_0^2 [\epsilon_r + \chi(N)] \vec{\mathcal{E}} = 0, \quad (3.5)$$

where $\chi(N)$ is a carrier density dependent “susceptibility” and ϵ_r is the relative effective index [23]. The addition of the susceptibility term assumes that all nonlinear effects can be modeled as a small perturbation to the dielectric permittivity, which can be complex. Substituting the field expression,

$$\vec{\mathcal{E}}(y, z) = \hat{a}_x Re\{\mathbb{E}(y)A(z)exp[j(\omega t - \beta z)]\}, \quad (3.6)$$

into the augmented Helmholtz’s equation, separating variables, and assuming a slowly varying envelope (i.e. $\partial_z^2 \ll \partial_z A$) produces

$$\frac{\partial A(z)}{\partial z} = j \frac{k_0^2}{2\beta} \chi(N) A(z) \quad (3.7)$$

$$\frac{\partial^2 \mathbb{E}}{\partial y^2} = (\beta^2 - k^2) \mathbb{E}. \quad (3.8)$$

From the latter equation, it is apparent that the modes of active and passive waveguides are solved for in the same manner (see the previous chapter).

To rewrite the former equation in a more useful expression, the susceptibility definition,

$$\chi(N) = j \frac{\beta}{k_0^2} g(N), \quad (3.9)$$

is substituted into equation 3.7. Multiplying by the conjugate of $A(z)$, produces the differential equation

$$\frac{\partial I}{\partial z} = gI = \frac{g_0 I}{1 + \frac{I}{I_{sat}}}, \quad (3.10)$$

which describes the field intensity over the length of an active waveguide. Integrating

over the amplifier length, L , and rearranging results in

$$\text{Gain}, G = \frac{I_{out}}{I_{in}} = \exp\left(g_0 L - \frac{I_{out} - I_{in}}{I_{sat}}\right), \quad (3.11)$$

which is a transcendental equation relating the input and output intensities. For the limiting case of the output intensity is far-below the saturation intensity (i.e. the gain is unsaturated), equation 3.11 reduces to

$$G_0 = \frac{I_{out}}{I_{in}} = \exp(g_0 L). \quad (3.12)$$

Figure 3.1 illustrates the numerical solution to equation 3.11 for a 10dB SOA and a 10dB saturable absorber (SA). In both scenarios, the gain (loss) quickly saturates when the input intensity nears the saturation intensity; ergo, the output intensity nears the input intensity as the input power increases, and conversely the intensity-dependent gain, g , becomes closer to its unsaturated value, g_0 , as the input power decreases (10dB and -10dB for the SOA and SA, respectively) .

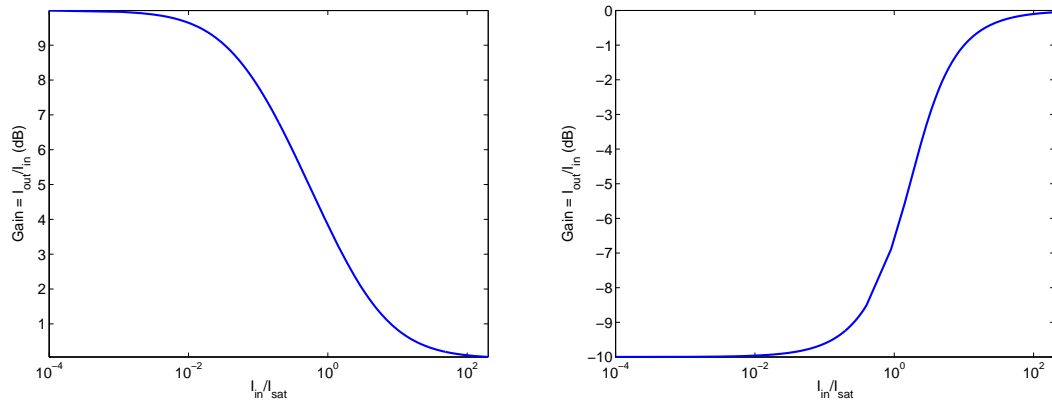


Figure 3.1: Gain versus input intensity solved numerically in MATLAB for a 10dB SOA (left) and a 10dB saturable absorber (right).

3.3 Phase Effects in Saturable, Active Media

Substituting equation 3.9 into 3.7 from the previous section, results in a differential equation describing the field amplitude-space relation:

$$\frac{\partial A(z)}{\partial z} = \frac{1}{2}gA(z). \quad (3.13)$$

In the previous section, $\chi(N)$ was assumed purely imaginary and defined as

$$\chi(N) = j\frac{\beta}{k_0^2}g(N). \quad (3.14)$$

Realistically, this is not exactly accurate and $\chi(N)$ needs an additional term to account for the phase shift imparted on the incident beam by the material. A more appropriate definition of the susceptibility is

$$\chi(N) = (j + \alpha)\frac{\beta}{k_0^2}g(N), \quad (3.15)$$

where α is known as the linewidth enhancement factor or the “Henry- α ” factor [23]. The linewidth enhancement factor is proportional to the ratio of the change in index of refraction and differential-gain with respect to the carrier concentration:

$$\alpha = -2k_0\frac{\frac{dn}{dN}}{\frac{dg}{dN}}, \quad (3.16)$$

in which n is the index, N is the injected carrier concentration in the active region, g is the differential gain, and k_0 is the free-space propagation constant [24, 25]. Unfortunately, calculating the “Henry- α ” factor is very difficult because it’s value is affected by such parameters as material, wavelength, and device structure; therefore, it is usually assigned a constant value (e.g. 4.7-5.5 for InP ridge waveguides [25]), which is experimentally verified [26].

Substituting the new definition of $\chi(N)$ into equation 3.7, results in

$$\frac{\partial A(z)}{\partial z} = \frac{1}{2}A(z)(1 + j\alpha)g, \quad (3.17)$$

which may be separated into two equations:

$$\frac{\partial A(z)}{\partial z} = \frac{1}{2}A(z)g \quad (3.18)$$

$$\frac{\partial \phi(z)}{\partial z} = \frac{1}{2}\alpha g. \quad (3.19)$$

This new form maintains $A(z)$ as just the field amplitude (i.e. without phase information) and ϕ contains all the phase information [23].

Chapter 4

Numerics

4.1 Overview of Numerical Techniques

Several techniques exist for modeling the propagation of light through linear and nonlinear materials, each with their own advantages and limitations. The most common modeling techniques fall into one of four archetypes: finite difference methods, “beam propagation” methods, finite-element methods, and modal analysis methods [12, 27].

The two most common finite-difference methods are the finite-difference beam propagation method (FD-BPM) and the finite-difference time-domain (FDTD) method. FD-BPM approximates the Helmholtz equation by a finite-difference equation. The exact abilities, accuracy, and stability of FD-BPM method are subject to which approximations are utilized such as the “Leapfrog” and trapezoidal method [28]. Various specialized methods exist to give enhanced functionalities to FD-BPM such as bidirectional propagation support [29, 30], incorporation of nonlinearities [31, 32], and stability with larger divergence angles [12, 33].

The finite-difference time domain method (FDTD), as its name implies, is a finite-difference method that also accounts for temporal dependencies. This method approximates each of Maxwell’s four equations with a finite-difference representation. Although this method is the most thorough and requires the fewest initial

assumptions, other methods are typically used, if possible, due to the enormous computational requirements [27].

Beam propagation methods (BPM) performs all calculations in Fourier space. The efficacy of computing Fast-Fourier Transforms (FFT) makes this method very fast, but the method has several disadvantages such as the inability to inherently incorporate polarization, necessity of fairly large discretization widths in the lateral direction, inability to properly simulate waveguides with large index contrasts, and necessity of equi-spaced discretization steps to name just a few [12, 27].

Finite-element methods receive their numerical efficiencies from utilizing small symmetric matrices in their calculations and the ability to handle complex waveguide designs readily [12, 27, 34]. Several varieties of the finite-element method exist to incorporate bidirectionality [35], nonlinearity [36, 37], and time-dependence [38].

Modal analysis methods solve for the modes of a waveguide and propagates each mode numerically separately. This method creates a huge reduction in numerical effort as the basis for calculations are a few modes instead of the entire Fourier spectrum. Modal analysis methods typically are designed for one specific architecture (e.g. ridge waveguide); thus, are not generally as flexible as other methods, but some modal methods such as radiation spectrum method (RSM), are designed to work with any arbitrary shape, account for both guided and radiative modes, and can even simulate such non-paraxial waveguides as Y-branches and bent waveguides [39].

For this work, a model was needed that could handle very weakly coupled waveguides, simulate saturable gain and loss, was fast enough to be run in MATLAB

(as to not necessitate its programming in a compiled language such as C), and was intuitively simple. At first, FD-BPM was utilized, but it was very slow in MATLAB and there were numerical instabilities resulting from the combination of active regions and the weakly-guiding nature of our waveguides. As an alternative, a modal analysis method was developed, which was numerically stable, fast, and took advantage a constant, symmetric geometry (a symmetric ridge waveguide).

4.2 Modal Propagation Analysis (MPA)

4.2.1 The Effective Index Method

Our waveguide structure is a ridge waveguide with a multiple-quantum well (MQW) active region as shown in figure 4.1, which is based on an existing active waveguide structure in Indium-Phosphide. The effective index method provides a method to represent the waveguide [cross-section] shown in figure 4.1 as a planar waveguide [11, 12, 13]. The effective index method separates the ridge-section of the waveguide from the cladding regions and finds an effective index for each section (see figure 4.2).

As an example, the effective index of the central section (the core) of the waveguide shown in figure 4.1 will be determined (see figure 4.3). Even though all electric fields in this work are TE polarized (in the x-direction in figures 4.1 and 4.2), the field is TM polarized ($H_z = 0, E_z \neq 0$) in each horizontal structure. The

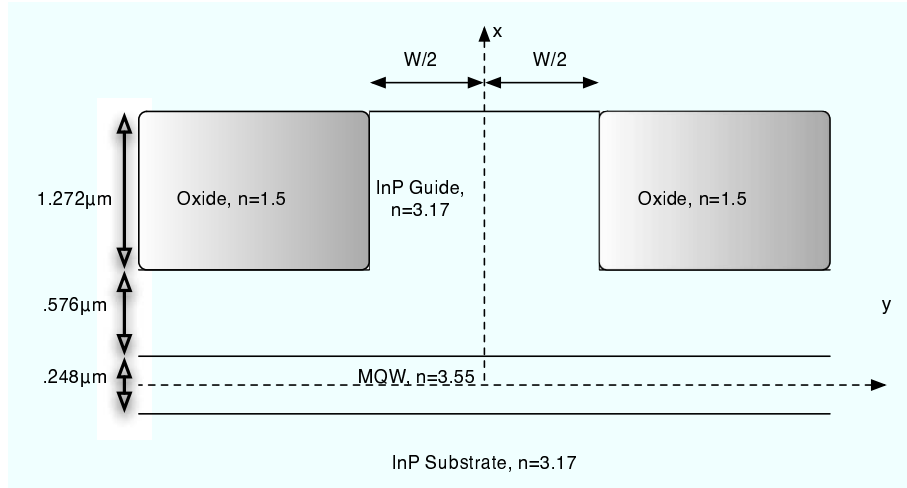


Figure 4.1: Cross-section of an active-core waveguide structure, which will serve as the basic geometry for all waveguides presented and simulated in this work.

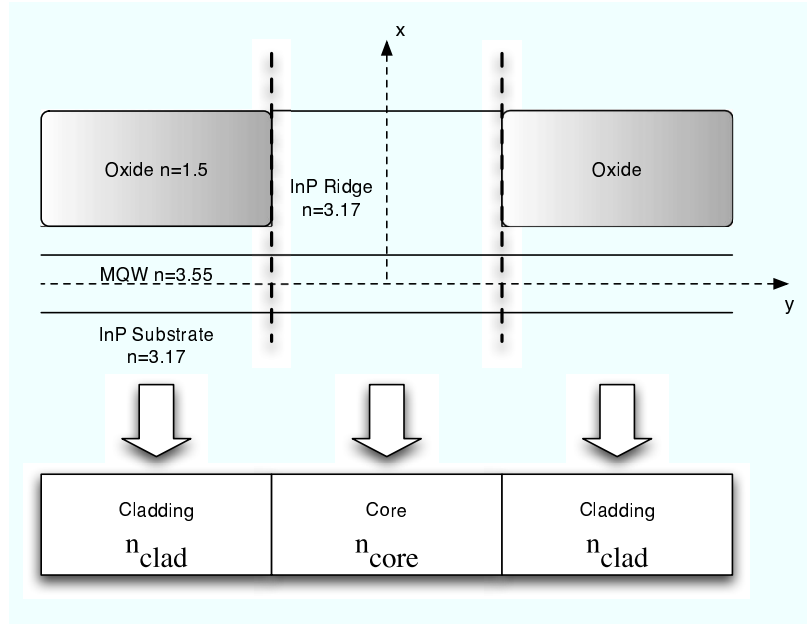


Figure 4.2: The effective index method approximates the layers of each segment of the waveguide by a single index of refraction. This device is divided into three regions and each is approximated separately.

guided modes of just the central segment of the waveguide are of the form

$$\mathbb{E}_z(x) = \begin{cases} Ae^{\alpha(x+\frac{d}{2})} & \text{if } x \leq -\frac{d}{2} \\ B \cos(\gamma x) + C \sin(\gamma x) & \text{if } -\frac{d}{2} \leq x \leq \frac{d}{2} \\ De^{-\alpha(x-\frac{d}{2})} & \text{if } x \geq \frac{d}{2}, \end{cases} \quad (4.1)$$

which is identical to the guided modes a symmetric planar waveguide (see chapter 2). In this equation d is the full height of the multiple-quantum well (MQW) layer and the electric-field is in the z -direction (direction of propagation). The tangential components of fields are continuous across boundaries; therefore, the z -component of the electric field will be continuous as well as the y -component of the magnetic field [10]

$$\mathbb{H}_y(x) = \begin{cases} \frac{j\omega n_{clad}^2}{\alpha} A e^{\alpha(x+\frac{d}{2})} & \text{if } y \leq -\frac{d}{2} \\ \frac{-j\omega n_{core}^2}{\gamma} [-B \sin(\gamma y) + C \cos(\gamma y)] & \text{if } -\frac{d}{2} \leq y \leq \frac{d}{2} \\ \frac{-j\omega n_{clad}^2}{\alpha} D e^{-\alpha(y-\frac{d}{2})} & \text{if } y \geq \frac{d}{2}. \end{cases} \quad (4.2)$$

Matching the boundary conditions of both the electric and magnetic fields, produces a transcendental equation

$$\tan\left(\gamma \frac{d}{2}\right) = \frac{n_{core}^2}{n_{clad}^2} \frac{\alpha}{\gamma}, \quad (4.3)$$

in which $\alpha^2 = \beta^2 - k_0^2 n_{clad}^2$ and $\gamma^2 = k_0^2 n_{core}^2 - \beta^2$. The largest β solution, which corresponds to the lowest-order mode, allows the calculation of the effective index, which is defined as

$$n_{eff} = \frac{\beta}{k_0}. \quad (4.4)$$

The effective index of the center-section of the waveguide structure drawn in figure 4.1 is approximately 3.285. A similar procedure is used for the cladding regions except there are 4 layers and thus 4 regions in which the fields' boundary

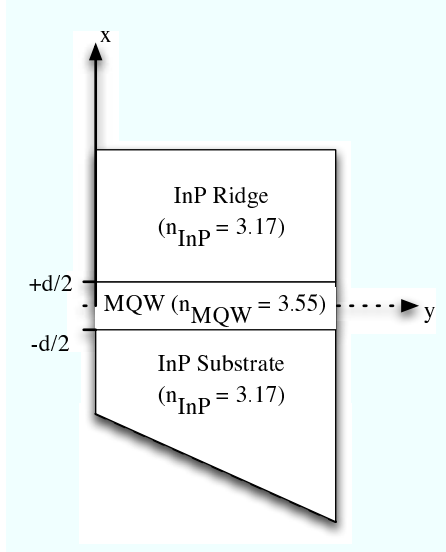


Figure 4.3: To determine the effective index of the central section of the waveguide drawn in figure 4.1, the segment is analyzed separately. The effective index of this segment is determined by observing the continuity of fields across each layer and determining the longitudinal propagation constant of the lowest-order guided TM mode propagating through just this section of the waveguide.

conditions are matched (only the quantum well region has a sinusoidal field and the remaining 3 regions have exponential fields). The effective index of the cladding region is approximately 3.2833. Software such as at [14] and [15] provides a way of determining effective indices of ridge waveguides.

4.2.2 Modal Solutions

With an index contrast of only .052%, the waveguide is considered “weak” and requires a sizable width to support multimode operation. Substituting the expressions for α and γ into the transcendental equations for the symmetric and antisymmetric guided modes (see Chapter 2), the propagation constants of each individual mode, β_ν , can be numerically determined. Graphically, the left and right-hand sides of equations 2.12 and 2.13 are shown in figure 4.2 for a $20\mu m$ wide waveguide. The

three points of intersection translate into three supported, guided modes: two symmetric and one asymmetric. The locations at which the plots of the left-hand sides of equations 2.12 and 2.13 intersect the horizontal axis, determine the γ whence each mode becomes supported (e.g. the first asymmetric mode becomes supported when γ is approximately 1.6×10^5). Table 4.1 shows (more accurately) the number of modes supported by a waveguide with respect to the core width.

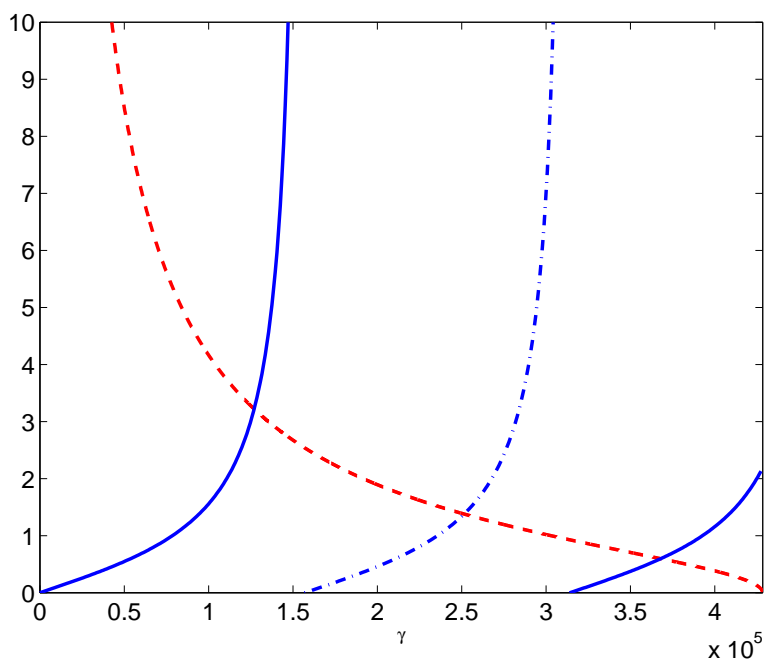


Figure 4.4: Plots of the left-hand sides of equations 4.1 (solid) and 4.2 (dot-dash) and the right-hand sides, which are the same (dash).

Graphically determining the individual modal propagation constants from the intersection points is neither accurate nor realistic, especially when hundreds of closely spaced modes are involved. It is also inaccurate, as was determined in our research efforts, to roughly approximate each propagation constant and then sequentially force orthogonality between each mode by systematically subtracting the

Modes Supported	Maximum Waveguide Width
1	7.3 μm
2	14.6 μm
3	22.0 μm
4	29.3 μm
\vdots	...
10	73.3 μm

Table 4.1: The maximum waveguide width before another mode becomes supported for a waveguide as shown in figure 4.1 with $n_{core} = 3.285$ and $n_{clad} = 3.2833$.

non-orthogonal components between modes:

$$\psi_2 = \psi_2' - \frac{\int \psi_1 \cdot \psi_2'^* dy}{|\psi_1|^2} \psi_1. \quad (4.5)$$

Calculating the propagation constants of each mode, β_ν , requires the use of an accurate numerical technique such as the Newton-Raphson method [16]. With this method, the right-hand sides of equations 2.12 and 2.13 are subtracted from the left-hand sides (separately) and the method iteratively approximates the zero-point with increasing accuracy through each iteration. Using up to thirty iterations in our simulations to determine the propagation constants, the corresponding normalized modal vectors were orthonormal ($\int \psi_m \psi_n^* dy = \delta_{mn}$) to at least 9 decimal places.

The desired input waveguide is single-moded and efficiently couples incident light into the multimode waveguide. To maximize this coupling, the diffraction angle out of the input waveguide should be equal to or less than the complement of the critical angle between the core and cladding of the multimode waveguide. From Snell's Law, the critical angle is approximately 88.16 degrees; therefore, the

complement is 1.84 degrees. The diffraction angle (in radians) is approximately

$$\theta_{diff} \approx \frac{\lambda_0}{n_{core}W_{in}}, \quad (4.6)$$

where n_{core} is the core index of refraction, λ_0 is the light wavelength in free-space (1.55 μm for our purposes), and W_{in} is the width of the input waveguide. The input waveguide width corresponding to a 1.84 degrees diffraction angle is $14.67\mu m$, which supports multiple modes as seen in table 4.1. To determine the most efficient single-mode input coupling, the input waveguide width is varied and numerically simulated.

The electric field of the input guide (neglecting the time-dependent term, $e^{j\omega t}$) is of the form

$$\vec{\mathcal{E}}_{in}(y, z = 0) = \hat{a}_x \mathbb{E}_{in}(y) = \begin{cases} Ae^{\alpha_{sm}(y+\frac{a}{2})} & \text{if } y \leq -\frac{a}{2} \\ \mathbb{E}_0 \cos(\gamma_{sm}y) & \text{if } -\frac{a}{2} \leq y \leq \frac{a}{2} \\ Be^{-\alpha_{sm}(y-\frac{a}{2})} & \text{if } y \geq \frac{a}{2}, \end{cases} \quad (4.7)$$

in which the coefficients A and B maintain the continuity of the field across the boundary (e.g. $A = \mathbb{E}_0 \cos(\gamma_{sm}d/2)$) and a is the input waveguide full-width. The normalized amplitude of the electric field in a $2\mu m$ waveguide is shown in figure 4.5.

Similarly, the expressions for the electric field of the symmetric and asymmetric

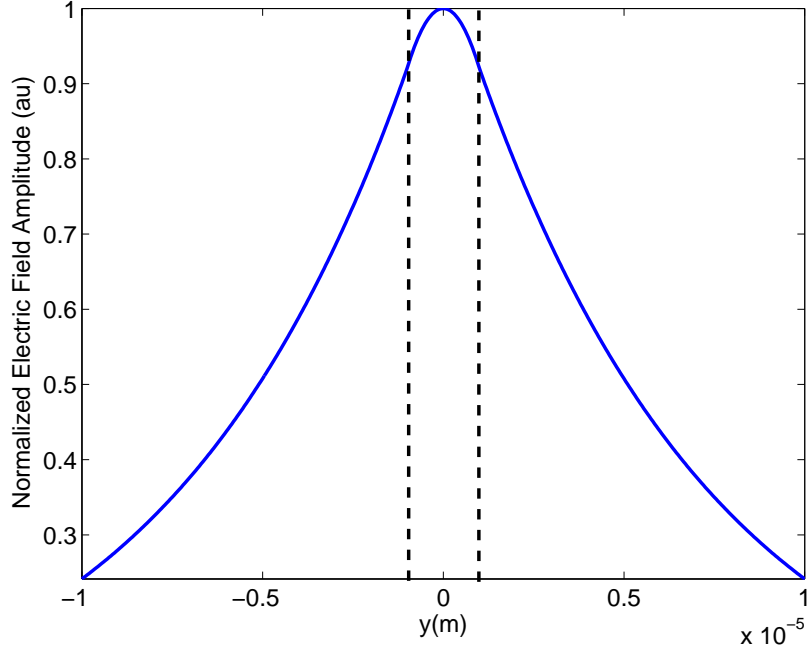


Figure 4.5: The normalized electric field pattern of the fundamental mode of a $2\mu\text{m}$ waveguide. The dashed lines represent the core-cladding boundaries.

modes (in that order) of the multimode waveguide are

$$\vec{\mathcal{E}}(y, z = 0) = \hat{a}_x \mathbb{E}_{Sym}(y) = \vec{a}_x \sum_i c_i \psi_i = \begin{cases} \sum_i A_i e^{\alpha_i(y + \frac{d}{2})} & \text{if } y \leq -\frac{d}{2} \\ \sum_i D_i \cos(\gamma_i y) & \text{if } -\frac{d}{2} \leq y \leq \frac{d}{2} \\ \sum_i H_i e^{-\alpha_i(y - \frac{d}{2})} & \text{if } y \geq \frac{d}{2} \end{cases} \quad (4.8)$$

$$\vec{\mathcal{E}}(y, z = 0) = \hat{a}_x \mathbb{E}_{Asym}(y) = \vec{a}_x \sum_m c_m \psi_m = \begin{cases} \sum_m J_m e^{\alpha_m(y + \frac{d}{2})} & \text{if } y \leq -\frac{d}{2} \\ \sum_m K_m \sin(\gamma_m y) & \text{if } -\frac{d}{2} \leq y \leq \frac{d}{2} \\ \sum_m M_m e^{-\alpha_m(y - \frac{d}{2})} & \text{if } y \geq \frac{d}{2}, \end{cases} \quad (4.9)$$

and the normalized modal amplitudes of a $28\mu\text{m}$ waveguide are demonstrated in figure 4.6. As before, the coefficients A, D, H, J, K, and M provide continuity between the electric fields at the boundaries for each individual mode, and the i - and m -subscripts refer to the i^{th} and m^{th} symmetric and asymmetric modes, respectively. The ψ 's are an orthonormal set representing the mode shapes of the electric field and the c 's are the coupling coefficients. The amount of electric field coupled into each mode from the input, single-mode waveguide is solved for via an overlap integral,

$$c_i = \frac{\int \mathbb{E}_{in}(y)\psi_i^*(y)dy}{\int |\mathbb{E}_{in}(y)|^2 dy}, \quad (4.10)$$

in which the i^{th} mode, in this case, may be any particular symmetric or asymmetric mode. In order to determine the most efficient input waveguide width, the total power coupled into the multimode waveguide is determined as the input waveguide is relocated away from the center of device (see figure 4.7).

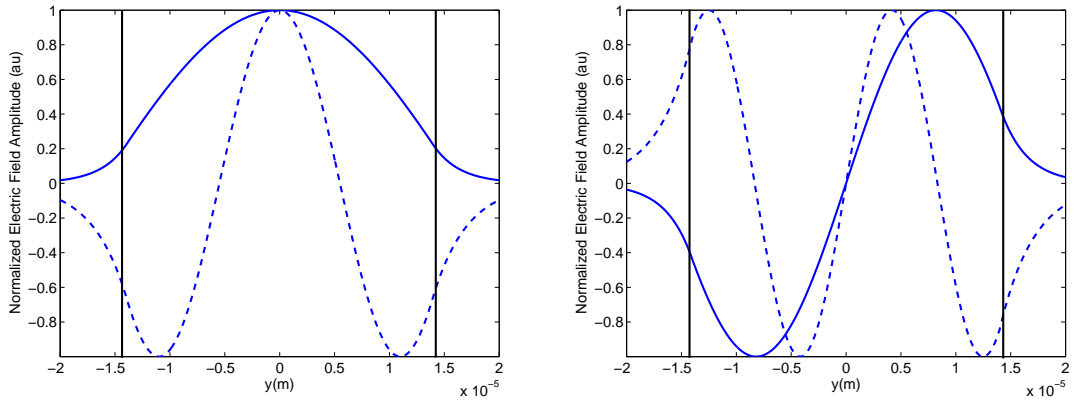


Figure 4.6: The two symmetric (left) and asymmetric (right) normalized mode patterns for a $28\mu\text{m}$ wide waveguide. The solid curves represent the lowest order symmetric/asymmetric mode and the dashed represents the highest (second in this case) symmetric/asymmetric mode. The solid vertical bars show the location of the core-cladding boundaries.

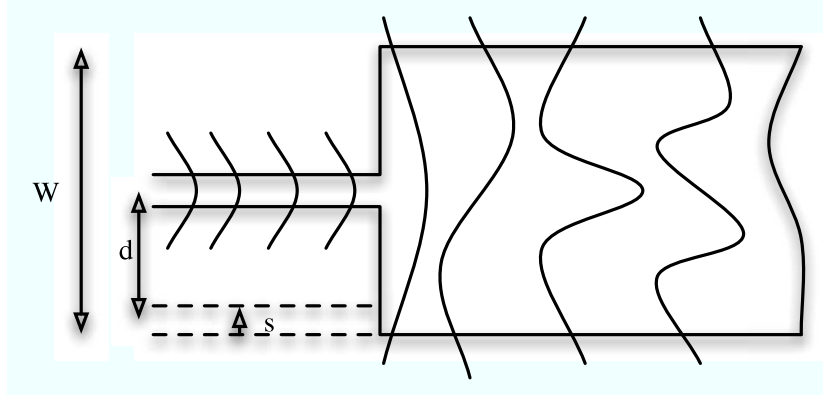


Figure 4.7: Drawing of a multimode waveguide with a varying input waveguide location. The ideal mode-shapes of both waveguides are superimposed atop each section of the guide. The input waveguide is single-moded and the MMI has four mode: two symmetric and two asymmetric.

For this investigation, the incident beam is the fundamental mode of the input waveguide, and the core and cladding of both the input and multimode waveguide are assumed lossless. The numerical results from simulating the power-coupling from the input to the multimode waveguide while varying the input waveguide width and location are shown in figure 4.8.

From figure 4.8, one can see that the most efficient coupling occurs for an input waveguide width between 2 and $3 \mu m$ until the waveguide gets very close to the edge of the device. Input coupling is greater than 95% for a $2 \mu m$ input waveguide, regardless of its location along the front-face of the multimode waveguide; therefore, all the simulations and designs in this work will use $2 \mu m$ input waveguides.

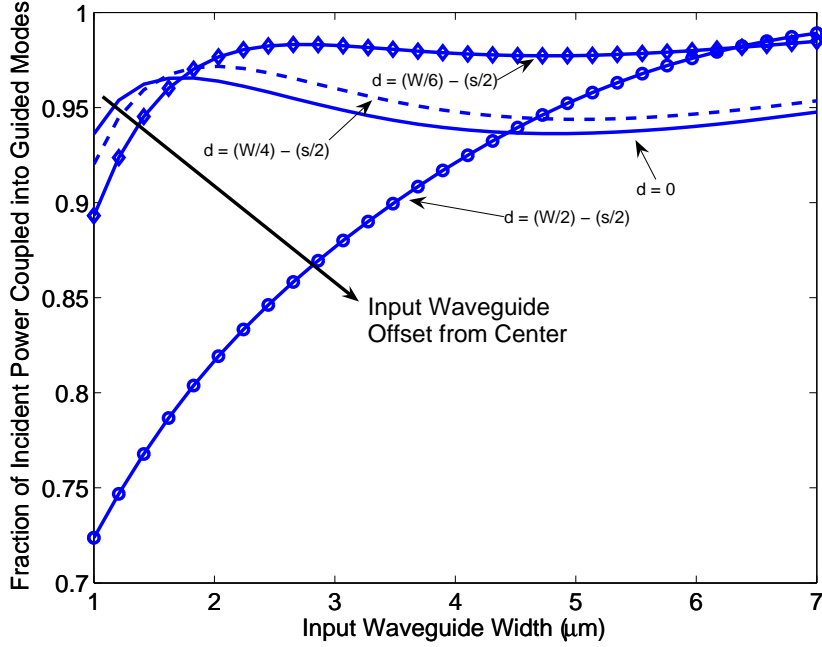


Figure 4.8: These traces show the fraction of input power coupled into guided modes versus input waveguide width. Three different input waveguide positions were simulated: centered (solid), halfway (dash) between the center and the edge of the MMI, a third away from the edge (diamonds), and flush with the edge of the MMI's core (circles).

4.2.3 Modal Propagation Analysis

Modal Propagation Analysis (MPA) assumes that all the individual modes are uncoupled from each other and the electric field propagates as

$$\mathbb{E}(y, z) = \sum_i c_i \psi_i e^{j(\beta_0 - \beta_i)z} + \sum_m c_m \psi_m e^{j(\beta_0 - \beta_m)z}, \quad (4.11)$$

where i and m represent the i^{th} and m^{th} symmetric and asymmetric mode (respectively), β_0 is the propagation constant of the fundamental mode i.e. lowest-order symmetric mode, and once again the $e^{j\omega t}$ term is implicit. For our first MPA simulation, the MMI is $28 \mu\text{m}$ wide with a centered, $2 \mu\text{m}$ input and core and cladding

refractive indices of 3.285 and 3.2833, respectively. From chapter 2, the approximate mirror-imaging length is 2.2mm, which agrees with the simulation output shown in figure 4.9 [17].

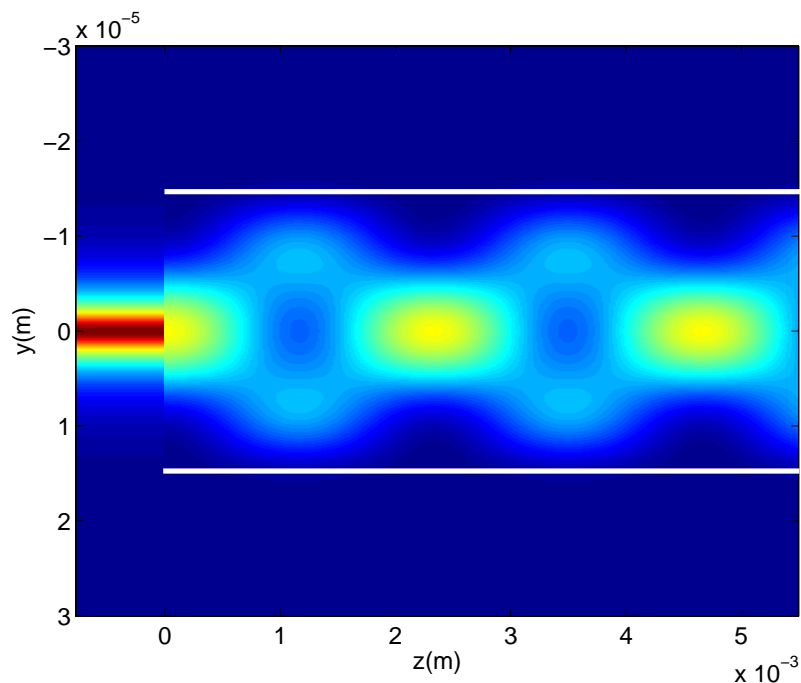


Figure 4.9: MPA simulation of light propagating through a .76mm long $2\mu m$ wide input waveguide and then coupling into a 5.5mm long, $28\mu m$ wide MMI. This waveguide supports four guided modes and is “weakly” guiding. White bars have been superimposed on the image to denote the (approximate) boundary between the core and cladding regions of the multimode waveguide.

Analyzing figure 4.9 presents some insights into the use of MPA for the chosen waveguide. Clearly there is a sudden change in the electric field intensity at the interface between the input and the multimode waveguides. The most probable cause of this unphysical result is due to the “weakly” guiding nature of the waveguide: the small index contrast between the core and cladding results in a sizable amount of light being coupled into non-guiding modes. If this is an accurate prognosis and the device is re-simulated with a larger index contrast, the sudden field change should

be replaced by a more-expected diffraction of the incident beam (see figure 4.10).

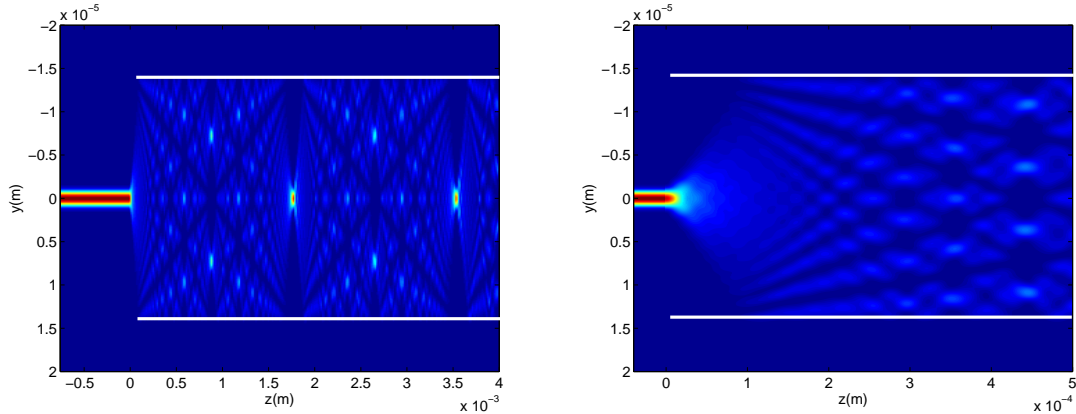


Figure 4.10: MPA simulation of light propagating through a .76mm long $2\mu\text{m}$ wide input waveguide and then coupling into a 5.5mm long, $28\mu\text{m}$ wide MMI. This waveguide has an index contrast of 1.7%, and supports twenty-two modes (eleven symmetric and asymmetric). White bars have been superimposed on the image to denote the (approximate) boundary between the core and cladding regions of the multi-mode waveguide. The figure on the right zooms in on the single-mode, multi-mode interface to demonstrate the diffraction of the beam.

This simulation with higher index-contrast (about 1.7%) demonstrates an image length of 1.76mm and an expected slit-diffraction of the field intensity as it escapes the single-mode waveguide and enters the multimode section. Clearly, the MPA method, when simulating a weakly-guided waveguide, needs to be augmented to account for the radiated energy as well.

4.3 Modal Analysis with Radiative Modes

4.3.1 Radiative Modes

As described in chapter 2, the radiated energy in a waveguide is calculated from a solution to the Helmholtz equation. Unlike the guided mode case, in which the core has a sinusoidal solution and the cladding's is evanescent, the radiation mode

solutions are sinusoidal in all regions (for a symmetric, ridge waveguide):

$$\mathbb{E}_{rx}(y) = \vec{a}_x \sum_j c_j \psi_j = \begin{cases} \sum_j A_j \sin[\alpha_j(y + \frac{d}{2})] + B_j \cos[\alpha_j(y + \frac{d}{2})] & \text{if } y \leq -\frac{d}{2} \\ \sum_j D_j \sin(\gamma_j y) + F_j \cos(\gamma_j y) & \text{if } -\frac{d}{2} \leq y \leq \frac{d}{2} \\ \sum_j G_j \sin[\alpha_j(y - \frac{d}{2})] + H_j \cos[\alpha_j(y - \frac{d}{2})] & \text{if } y \geq \frac{d}{2}. \end{cases} \quad (4.12)$$

The solution to the Helmholtz equation for radiative modes produces an infinite set of longitudinal propagation constants, β . Like the guided modes, the radiative modes corresponding to these β 's form an orthogonal set with each other and the guided modes, but only in infinite space; therefore, a method need be constructed to properly select which radiative modes to incorporate in simulations and how to normalize the individual mode shapes, ψ_i , so that energy is conserved in the model. One such common method in modal analysis models is to impart an artificial Neumann or Dirichlet boundary condition at the simulation window's edge and to normalize the modes over this window:

$$\psi_i(y) = \frac{\psi'_i(y)}{\sqrt{\int_{-W_{sw}/2}^{W_{sw}/2} \psi'_i(y) dy}}, \quad (4.13)$$

where ψ'_i is the un-normalized mode shape of the i^{th} radiated mode and W_{sw} is the full simulation window width. This normalization scheme (the same as that used for the guided modes) insures that that the set of all modes (guided and radiative) form an orthonormal set over the simulation window, but the size of the boundary window need be carefully selected. To find the simulation window width in which

the guided mode solutions are nearly-unperturbed, we numerically find the γ 's from the guided-mode solution to the Helmholtz equation with the additional Dirichlet boundary conditions at the simulation window width. Figure 4.11 compares the percentage difference between the γ solutions for the ideal infinite-window solution, $\gamma_{infinite}$, and the new solution with a bound window, γ_{bound} , for the “weakly” guiding $28\mu m$ wide waveguide that is center-fed from a $2\mu m$ waveguide.

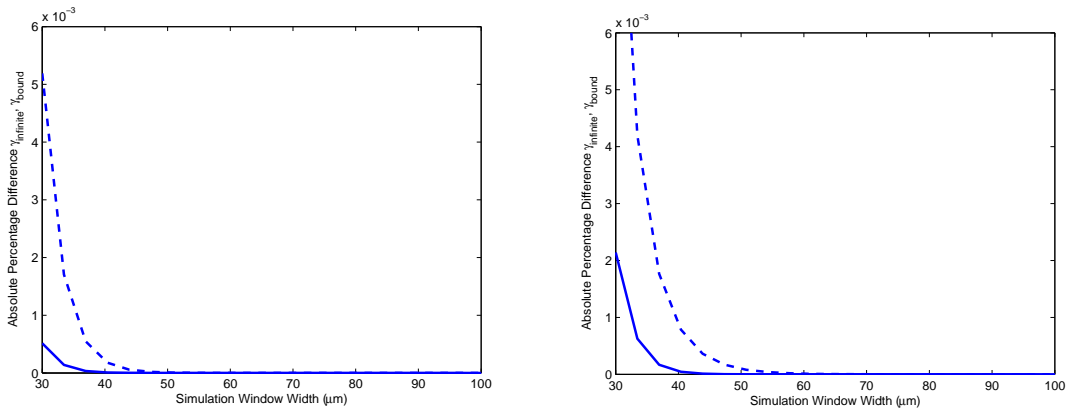


Figure 4.11: The absolute percentage difference between the infinite-window and bound-window γ solutions for the symmetric (left) and asymmetric (right) modes. The solid-line plots are the lower-order modes and the dashed the higher.

For the symmetric mode solutions, the modal perturbation minimizes for a simulation window of greater than approximately $50\mu m$ and $60\mu m$ for the asymmetric solutions. Numerically calculated, the power coupling into the waveguide with a simulation window of $60\mu m$ results in 99.9961% of the incident field intensity being coupled into a mode (guided or radiative) for the input waveguide at the edge of the MMI, and this efficiency increases to 99.99989% for center-fed. With efficiency this close to 1, the boundary window does not need to be expanded further. Figure 4.12 shows the input field intensity profile versus the intensity coupled into

the multimode waveguide from a centered input – including and excluding radiative modes.

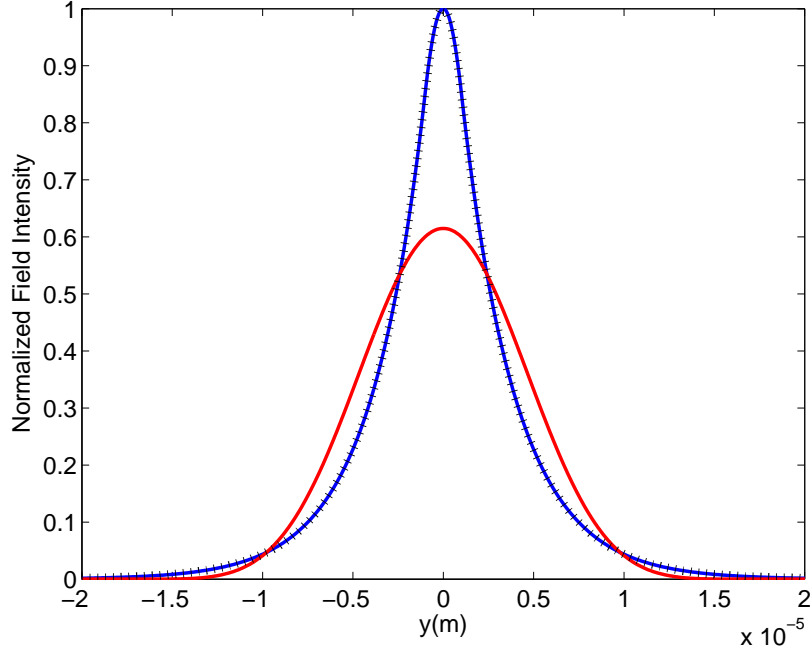


Figure 4.12: Normalized field intensity profile before (solid) and after coupling into the multimode waveguide from the single-mode input. The field intensity from incorporating guiding modes is shown with a dashed line, and the profile including radiative modes are cross-hatches. The field intensity profile coupled into guided and radiative modes accounts for nearly 100% of the total incident power; thus, the cross-hatches lie directly on top of the incident beam profile.

Figure 4.13 demonstrates MPA with radiative modes for a multimode waveguide in the case of a centered and an offset input. The *choppy* distortions (especially apparent in the offset-input case) are caused by numerical reflection, because the Dirichlet boundary conditions at the simulation-boundary window’s edges represent perfect reflectors. These numerical reflections are a common difficulty in all numerical simulation method, whether using modal analyzers such as MPA or RSM, or finite-difference method such as FD-BPM or FDTD. The oldest solution to this

problem was to ignore all β 's associated with a mode that would reflect off the simulation boundary at the expense of lost energy. From a ray-optics perspective, the angle of a mode's propagation (relative to the propagation axis) in the core and cladding, respectively, is

$$\theta_{core} = \cos^{-1} \frac{\beta}{k_{core}} \quad (4.14)$$

$$\theta_{clad} = \cos^{-1} \frac{\beta}{k_{clad}}, \quad (4.15)$$

which is graphically shown in figure 4.14. If the radiative modes, which will reflect at the boundaries, are ignored in the simulations demonstrated in figure 4.13, only four modes remain. Unfortunately, these modes do not contain the power or numbers to demonstrate the benefits of using radiative modes.

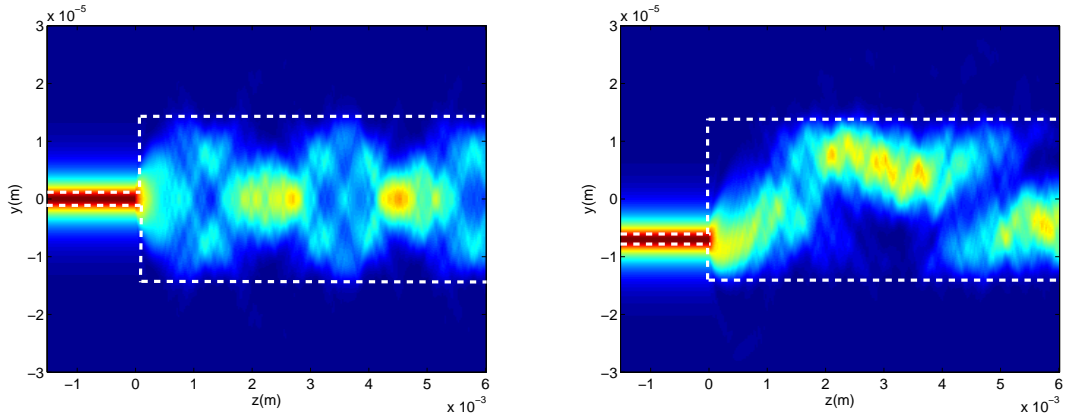


Figure 4.13: MPA simulation of a $28\mu m$ waveguide with radiative modes included. The left-hand figure demonstrates this multimode waveguide with a $2\mu m$ input waveguide centered on the front-face. The right-hand simulation is excited via a $2\mu m$ input waveguide offset by $7\mu m$ from the center of the front-face. The *choppy* distortions are caused by the radiative modes' energy reflecting off of the boundary window, which was given an artificial Dirichlet condition.

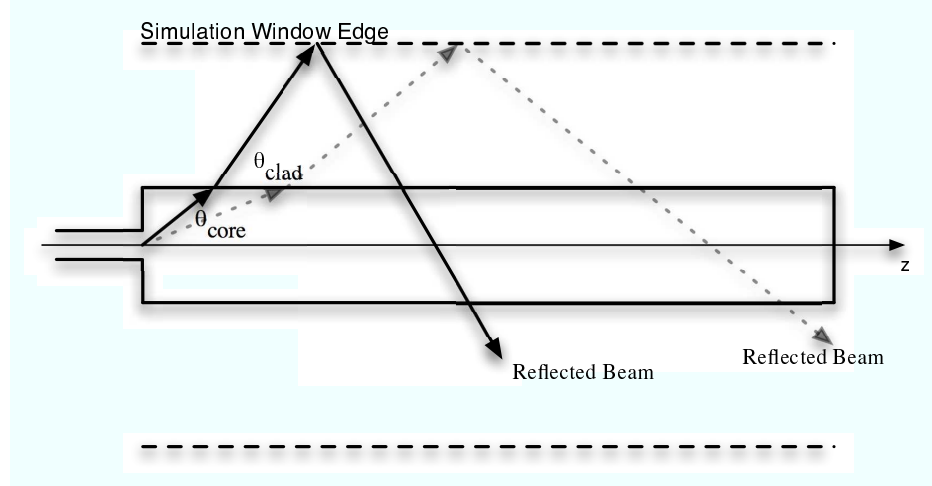


Figure 4.14: With Dirichlet boundary conditions enforced on the simulation windows' boundaries, the radiative modes will reflect at the boundary. This figure shows the reflection of two different radiation modes (solid and dashed)

4.3.2 Reducing Simulation Window Reflections via the Virtual Boundary Condition (VBC)

Common techniques to reduce reflections in finite-difference methods are absorbing boundary conditions (ABC), in which an artificially and slowly absorbing layer is placed between the edge of the waveguide and the simulation window and transparent boundary conditions (TBC), in which a perfect matched layer (PML) is implemented at the edge of the simulation window [12, 17]. Unfortunately, these methods are not implementable in modal analysis methods; therefore, a different approach needs to be taken.

To prevent boundary reflections, the radiative modes are discretized in a different method than simply implementing Dirichlet boundary conditions at the simulation windows' edges. One such method is the radiation spectrum method (RSM) [39], in which an arbitrary number of equally-spaced β 's are selected between the

minimum value for radiative modes, 0, and the maximum value, k_{clad} :

$$\beta_i = i \frac{k_{clad}}{N} \quad i = 0, 1, 2, \dots, N-1, \quad (4.16)$$

where N is an arbitrary integer.

Another method is to select β 's using a Lanczos-Fourier expansion [40]. These methods reduce reflections in the simulation because the individual modes do not equal zero at the simulation boundary; therefore, there is no perfect reflector. In both of these techniques there can still be reflections; therefore, certain conditions exist for each technique in order to only select modes, which will not reflect. Also, the individual modes in both these methods are not necessarily orthonormal over the simulation window and have to be specially normalized to maintain energy conservation. For this work, another discretization scheme was developed: virtual boundary conditions (VBC).

With VBC the Dirichlet boundary conditions are implemented, but at a distance much greater than the simulation boundary window i.e. at a virtual boundary (see figure 4.15). The specific propagation constants for the radiative modes are found by numerically solving the Helmholtz equation with Dirichlet boundary conditions at the virtual boundary. Even with this method, the β 's that will result in reflected energy entering the MMI within the simulation length are thrown-out, but selecting any virtual boundary larger than the simulation window will result in a larger number of β 's, which do not completely reflect back into the device before the end of the device; therefore, more radiative modes can be simulated. Previously

each mode was normalized over the width of the simulation boundary:

$$\psi_i(y) = \frac{\psi_i'(y)}{\sqrt{\int_{-W_{sw}/2}^{W_{sw}/2} \psi_i'(y) dy}}, \quad (4.17)$$

where $\psi_i'(y)$ is the un-normalized shape of mode i , $\psi_i(y)$ is the normalized mode, and W_{sw} is the full-width of the simulation window. For our new simulations with VBC, the radiative modes inside the computational window are normalized to the mode shapes extending to the VBC:

$$\psi_i(y) = \frac{\psi_i'(y)}{\sqrt{\int_{-W_{VBC}/2}^{W_{VBC}/2} \psi_i'(y) dy}}, \quad (4.18)$$

in which W_{VBC} is the full-width of the virtual boundary, ψ_i'' is the i^{th} mode extending to the virtual boundaries, and ψ_i' is the i^{th} mode extending just to the computational window boundaries.

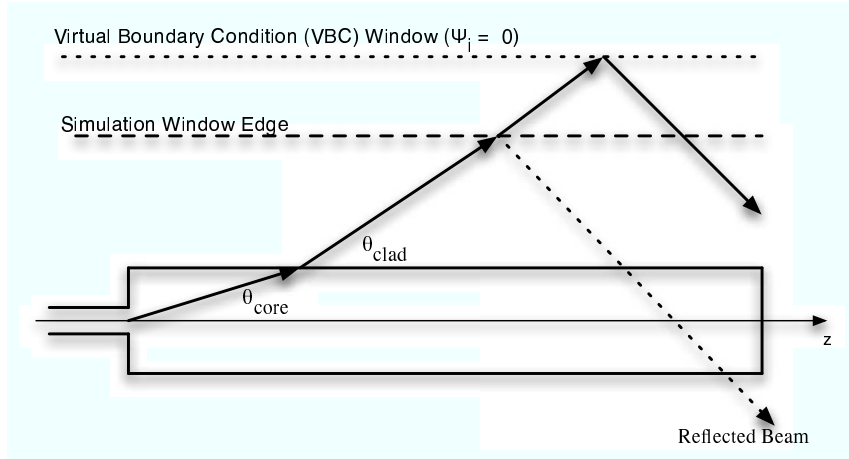


Figure 4.15: The rays demonstrate the propagation of one radiative mode if Dirichlet conditions were imposed on the simulation boundary window (dotted) or at a virtual boundary (solid). With VBC, the same radiative mode can be simulated without concern over numerical reflections.

This method is much faster than simply increasing the simulation window boundary, because the floating-point operations per second (FLOPS) in simulating just the linear propagation is directly proportional to the length of each one-dimension mode vector. The difference in flops between expanding the actual simulation boundary and the virtual one (*ceteris paribus*) is further accentuated in the nonlinear region, which will be discussed in section 4.4, in which the FLOPS are proportional to the vector length to the fourth power.

As shown in figure 4.16, re-simulating the $28\mu\text{m}$ wide, 6mm long MMI with VBC demonstrates no reflection interference even though 370 radiative modes were used. The VBC was selected at $750\mu\text{m}$ and the input power coupled was 99.9993%. The power at the output of the simulation was approximately 97.37%, which demonstrates that almost all the radiated power had escaped the MMI and not returned due to numerical reflections.

4.4 Modal Propagation Analysis with Nonlinearities Incorporated

As presented in Chapter 3, three equations that describe wave propagation through an active, saturable medium are

$$\frac{\partial I(y, z)}{\partial z} = g(I)I(y, z) \quad (4.19)$$

$$\frac{\partial \phi(y, z)}{\partial z} = \frac{1}{2}\alpha g(I) \quad (4.20)$$

$$g(I) = \frac{g_0}{1 + \frac{I(y, z)}{I_{\text{sat}}}} \quad (4.21)$$

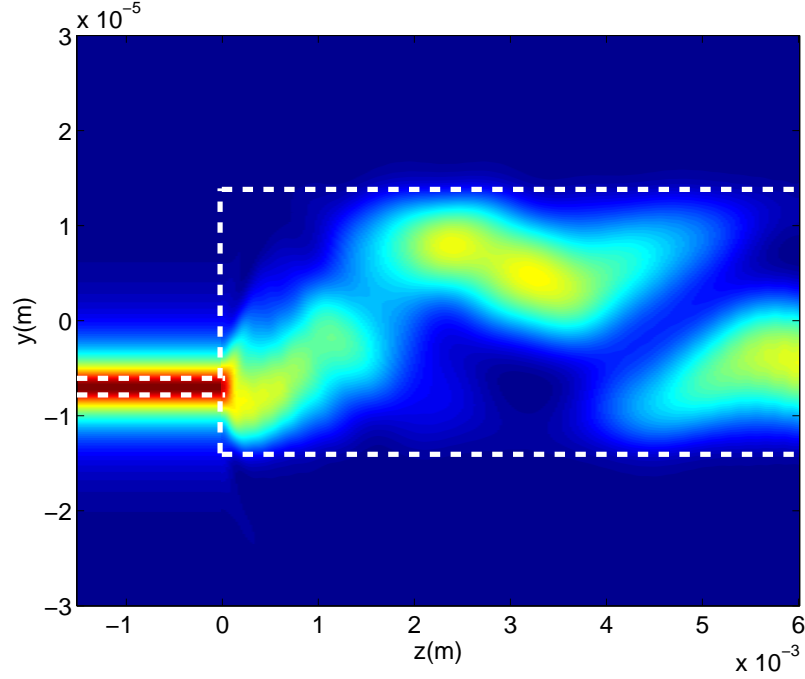


Figure 4.16: The simulation of a $28\mu m$ multimode waveguide with a $2\mu m$ input waveguide offset by $7\mu m$. This simulation utilized a $750\mu m$ VBC so that over 350 radiative modes are supported and there are no numerical reflections at the simulation windows' boundaries.

where $I(y, z)$ is the light intensity, $g(I)$ is the saturable gain/loss function, g_0 is the unsaturated gain, α is the linewidth enhancement factor, and I_{sat} is the saturation intensity. As was also mentioned in chapter 3, equation 4.14 is a transcendental equation; therefore, a numerical technique needs to be used to find a solution. For our work we will use a split-step method and approximate the gain function as

$$g \approx \frac{g_0}{1 + \frac{I_{in}}{I_{sat}}}, \quad (4.22)$$

so that $I_{out} \approx I_{in} \exp(g(I_{in} \Delta z))$. In the previous equation I_{in} and I_{out} are the input and output intensity for one Δz step, respectively. This approximation is reasonable for small step sizes (Δz) as shown in figure 4.17. This figure shows that for a 2mm

long 30dB SOA, the approximation is reasonably accurate when Δz is smaller than $20\mu m$ and the output intensity is near the saturation intensity. This approximation is accurate for even larger Δz values as the input intensity becomes much smaller or greater than the saturation intensity.

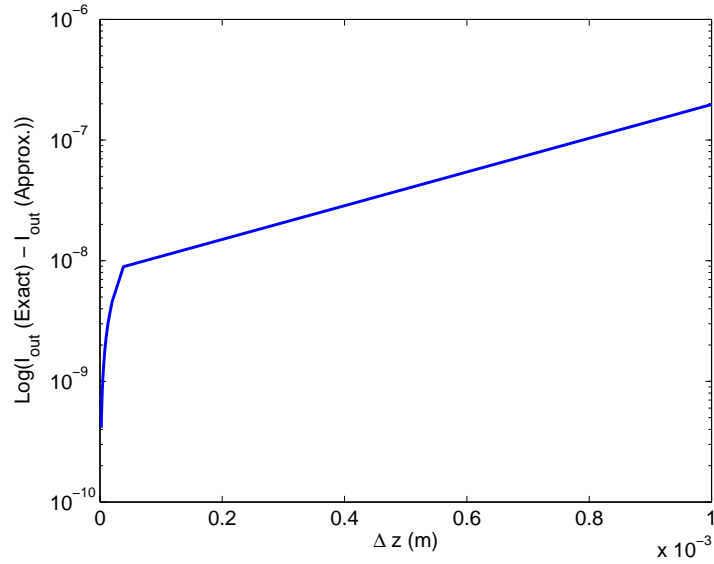


Figure 4.17: The intensity difference in a 2mm (1D) 30dB SOA between solving equation 4.16 numerically with the gain function as equation 4.18, $I_{out}(Exact)$, and approximating the gain function as equation 4.19, $I_{out}(Approx.)$, as a function of step-size, Δz

To allow larger step-sizes, an iterative method is implemented:

1. Evaluate the gain function for the input intensity, $I(z)$:

$$g = \frac{g_0}{1 + \frac{I(z)}{I_{sat}}} \quad (4.23)$$

2. Evaluate the output power, $I(z + \Delta z)$:

$$I(z + \Delta z) = I(z)e^{g*\Delta z} \quad (4.24)$$

3. Re-evaluate the gain using the just-calculated output power:

$$g = \frac{g_0}{1 + \frac{I(z+\Delta z)}{I_{sat}}} \quad (4.25)$$

4. Re-evaluate the output power:

$$I(z + \Delta z) = I(z)e^{g*\Delta z} \quad (4.26)$$

5. Repeat as desired.

As this technique is repeated, the re-evaluated gain will converge and no further improvement is obtainable. For particularly high-gain devices or with relatively large step sizes, more iterations of this technique are necessary. For our previously demonstrated SOA (30dB), the difference between the approximate solution and the exact solution diminishes by roughly two orders of magnitude even when the gain is only re-evaluated once as shown in figure 4.18. In balancing computation time and simulation accuracy, all further simulations in this work use one iteration.

In order to apply this method to the propagating light at each simulated step, a split-step method is used in which light is propagated one step, Δz , and then all gain/loss for that length is applied in an infinitesimally small width as shown in figure 4.19.

After each step the coupling coefficients for each mode are re-evaluated, because the gain and loss will perturb how much energy is in each guided and radiative mode. The assumption that our mode-shapes remain the same and only the cou-

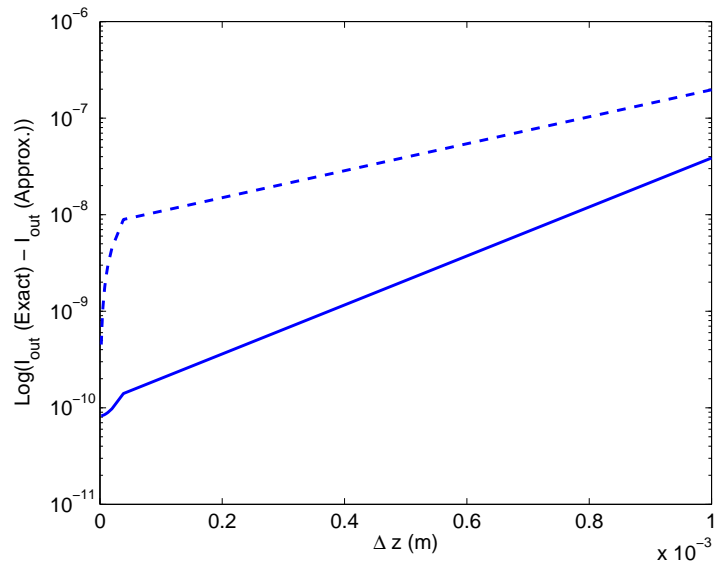


Figure 4.18: The intensity difference in a 2mm (1D) 30dB SOA between solving equation 4.16 numerically with the gain function as equation 4.18, $I_{out}(Exact)$, and approximating the gain function, $I_{out}(Approx.)$, as a function of Δz . The iterative method (solid) produces two orders of magnitude improvement over approximating the gain function as equation 4.19 (dashed).

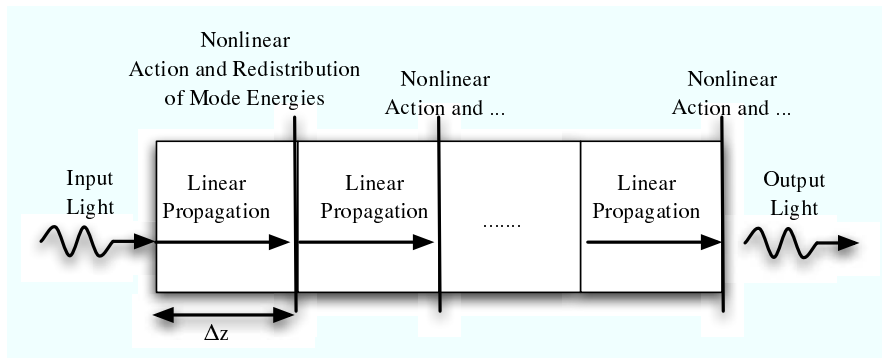


Figure 4.19: In a split-step method, light is linearly propagated one step, Δz , and then all nonlinear action (e.g. gain, loss, etc.) are performed in an infinitesimally small region. After each nonlinear step, the exact coupling of the fields into each eigenmode (guided and radiative) is re-determined via overlap integrals.

pling of energy changes is an appropriate approximation with the caveat that the gain/loss does not significantly perturb the effective index of the waveguide. In the

limiting case of unsaturated gain, the field through one step is

$$\mathbb{E}_x(y, z + \Delta z) = \mathbb{E}_x(y, z) \exp(j\omega t - j\beta\Delta z + j.5 * \alpha g_0 \Delta z + .5 * g_0 \Delta z). \quad (4.27)$$

One can see that as long as $\alpha g_0 \ll \beta$ the approximation is reasonable. For the simplest case in which the field is entirely in the fundamental guided mode, $\beta = k_{core} \approx 1.33 \times 10^7$ and $\alpha g_0 \approx 1.7 \times 10^4$ for a 30dB, 2mm long SOA with $\alpha = 5$; therefore, the perturbative approximation is reasonable. The cases in which β and αg_0 are reasonably close does not apply here as the energy will be coupled into radiative modes with very steep angles, which evacuate the device very quickly.

As an example, Figure 4.20 demonstrates the simulation of a 20dB SOA below and above saturation. From the simulation, the actual gain produced was 19.7dB, which includes input-coupling loss, for a peak input intensity of $10^{-20} I_{sat}$, and the gain at saturation was approximately -15dB for a peak-input of $10,000 I_{sat}$.

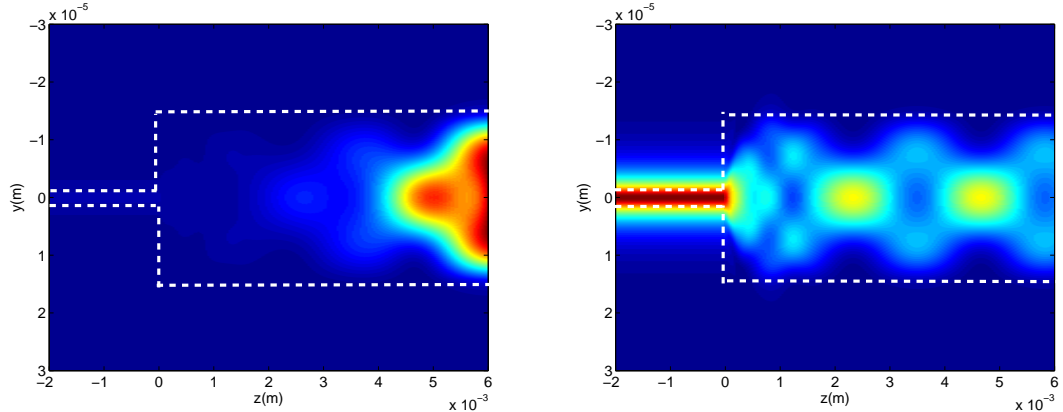


Figure 4.20: Simulation of a 20dB SOA below (left) and above (right) saturation. With intensities far below saturation, the gain was calculated to be 19.7dB. For intensities above saturation, the device's gain was approximately -15dB; thus, some energy was lost due to radiation and coupling losses.

Chapter 5

Patterned Active Region Multimode Switches (PARMS)

5.1 3-segment PARMS

Multimode interference semiconductor optical amplifiers (MMI-SOA) have experimentally demonstrated thresholding capabilities [7, 8]. The spatial non-uniformity of the field inside the device results in spatial variations in the intensity-dependent gain; thus, each mode is differently modulated. In these devices, the modes are not only amplified, but also receive an additional phase-shift. In these dual-output waveguide devices, this intensity-dependent phase shift switches the output power between the two output waveguides by modulating the relative phase between the odd and even modes [41]. With careful design the power switching creates an output port that performs as a thresholder for the input.

This chapter examines the performance of another multimode switch. As opposed to the MMI-SOA, which only provides spatially varying negative phase shift and uniform gain, the device proposed in this chapter contains electrically isolated gain and loss regions that provide spatially varying gain and loss as well as negative and positive phase shifts. In theory, the shape, size, and location of the individual active regions inside the multimode waveguide can be “patterned” to optimize the switching characteristics for thresholding; thus, these devices are termed “patterned active region multimode switches” (PARMS).

The first PARMs design is a $28\mu\text{m}$ wide multimode waveguide with a $2\mu\text{m}$ input waveguide set in between the center and the outer edge of the multimode waveguide (see figure 5.1). The 2.29mm length of the device corresponds to the optimized imaging length determined from numerical simulations. This device has three isolated active regions, which can be individually biased to create gain, loss, or transparency. Twin $2\mu\text{m}$ waveguides are fabricated to provide output coupling. For simplicity, power coupled into the output waveguide, which is in-line with the input waveguide, is said to be in the “bar” state, and light coupled into the other waveguide is in the “cross” state. The simulation of a field propagating through this device with input intensities much larger than saturation is shown in figure 5.2.

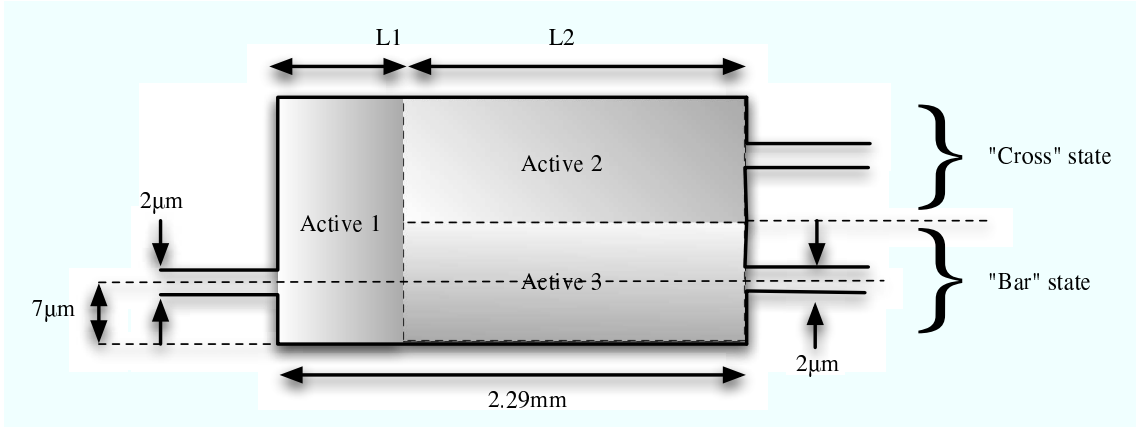


Figure 5.1: Schematic of a 3-segment PARMs with symmetric, single-mode output waveguides. These two waveguides, as simulated, are fabricated with the same process as the PARMs; thus, they are also weakly guiding, and are both offset from the center of the end-face by $7\mu\text{m}$ (from center-to-center).

For the initial simulation of power-switching, a device was designed with small gain (loss) below 5dB and with a linewidth enhancement factor of 5, which was selected based on reasonable values for Indium-Phosphide MQW structures [25]. To account for variabilities in the gain media, the intensities are normalized in the

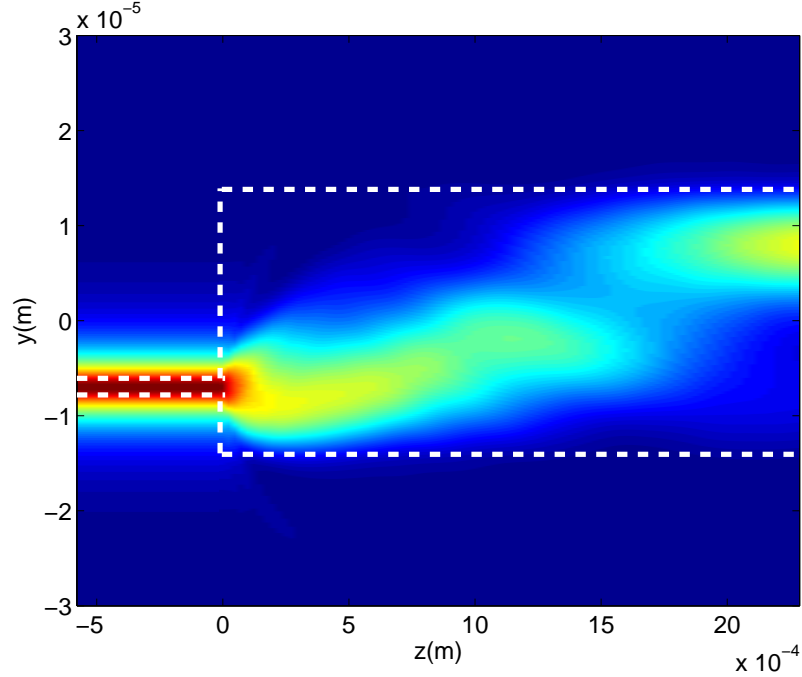


Figure 5.2: Simulation of an incident beam from a $7\mu m$ -offset, $2\mu m$ input waveguide into a $28\mu m$ multimode waveguide. The incident power is much higher than the saturation power for the active regions; therefore, the light propagates as if the waveguide were passive.

simulation algorithm with respect to the gain saturation intensity in the multimode waveguide and the loss saturation intensity is 57.89% of the gain saturation value. This value was selected from the work of Dr. Paul Petruzzi, whose dissertation included experimental testing of devices with similar materials and structure [42]. The device was simulated with lengths $L1 = .8375mm$ and $L2 = 1.454mm$ and the active regions designed for 0dB, -4dB, and +5dB of gain (see figure 5.3). The simulation of this device with input intensities far below saturation is shown in figure 5.4.

The gain (P_{out}/P_{in}) for each output waveguide versus input power is shown in figure 5.5. This gain function with its constant-gain response at low and high input

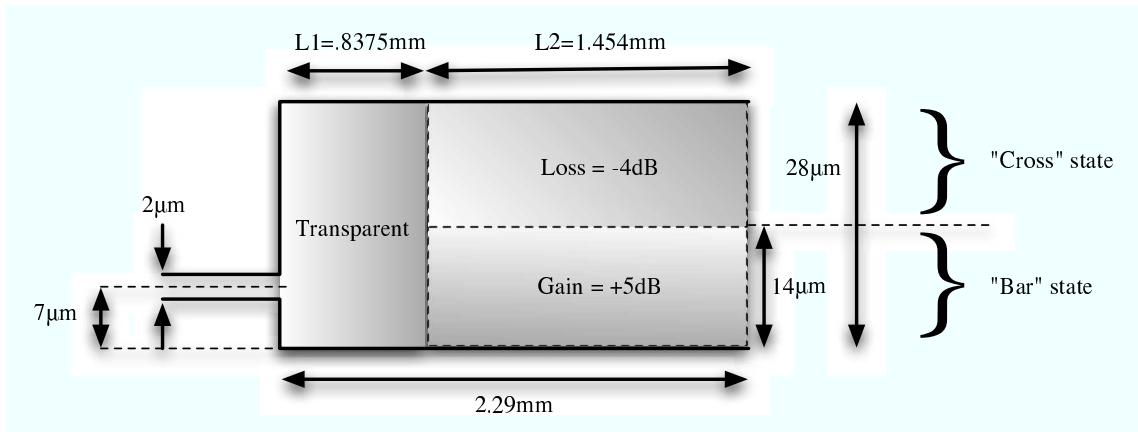


Figure 5.3: Schematic of a 3-segment PARMS with dimensions and values assigned.

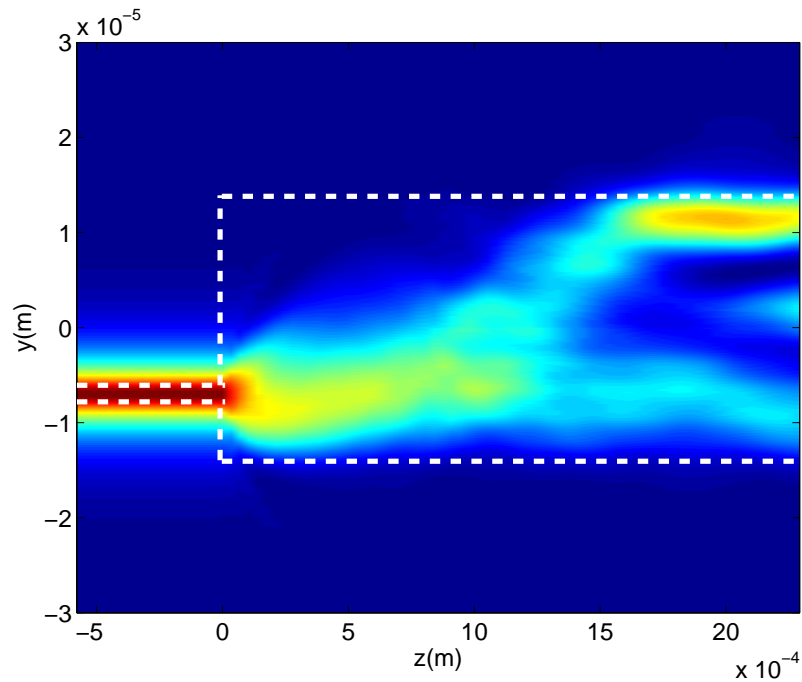


Figure 5.4: Simulation of the 3-segments PARMS shown in figure 5.4 for input intensities far below saturation. As shown, a portion of the total input power has switched over to the “bar” state at the output.

powers, which is a quality found similarly in single saturable absorbers (see chapter 1), produces output powers as shown in figure 5.6. The “bar” state output extinction ratio is roughly 5dB over an input span of approximately 5dB and the “cross” state output demonstrates similar characteristics. With their small output extinction

ratios and lack of discernible constant “high” or “low” state output power values, neither output performs adequately or noticeably better than a single saturable absorber.

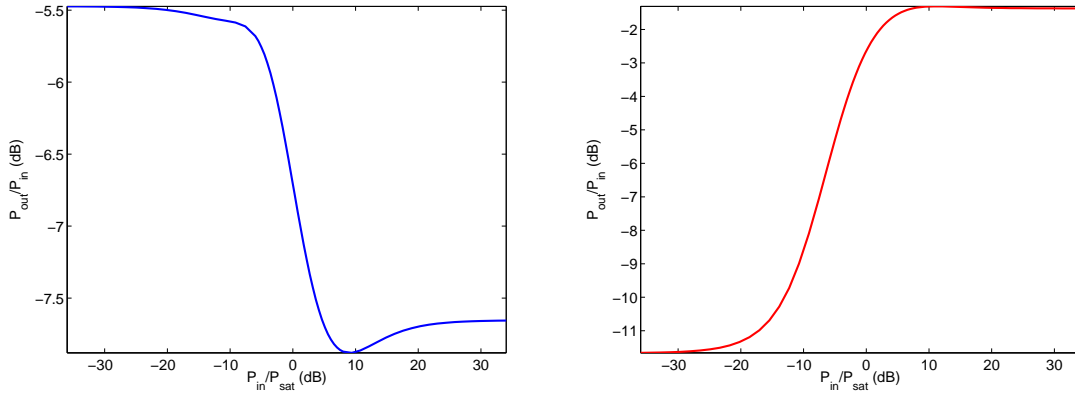


Figure 5.5: Gain versus input power for the bar (left) and cross (right) state output of the PARMS shown in figure 5.3.

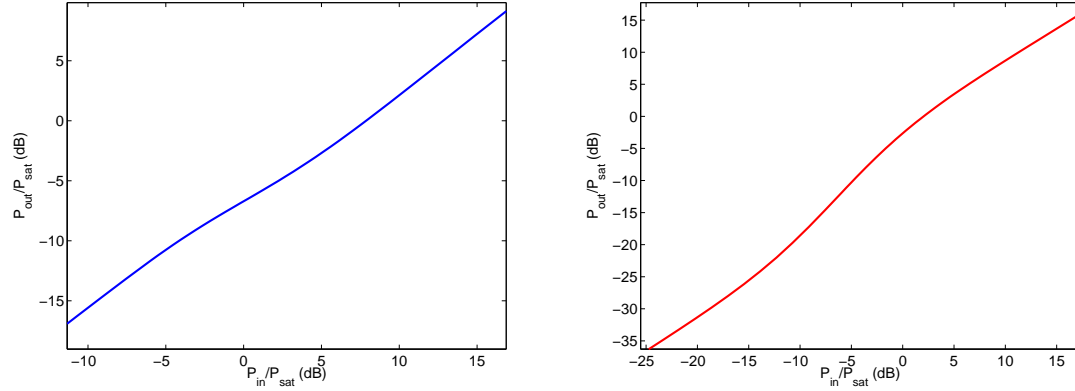


Figure 5.6: Output versus input power for the bar (left) and cross (right) state output of the PARMS shown in figure 5.3.

To create a more apt device, alterations are made to the gain and loss values of the active regions while maintaining the same geometry. The previously transparent region is changed into a -5dB loss segment, and the previous gain and loss segments are adjusted to +10dB and -20dB, respectively (see figure 5.8). The altered de-

vice’s outputs both act as thresholders as shown in figure 5.9. The “bar” state output thresholder performs with an extinction ratio of approximately 9dB over a 6dB input power span, and the “cross” state has an extinction ratio of 23dB over 6dB. Qualitatively, the “cross” state output’s transfer function is the better suited thresholder due to its larger extinction ratio, its *flatter* “low” state power curve, and its operational power span between approximately 0dB and 10dB. The cross state output does not completely flatten and thus it resembles a single saturable absorber at higher input intensities.

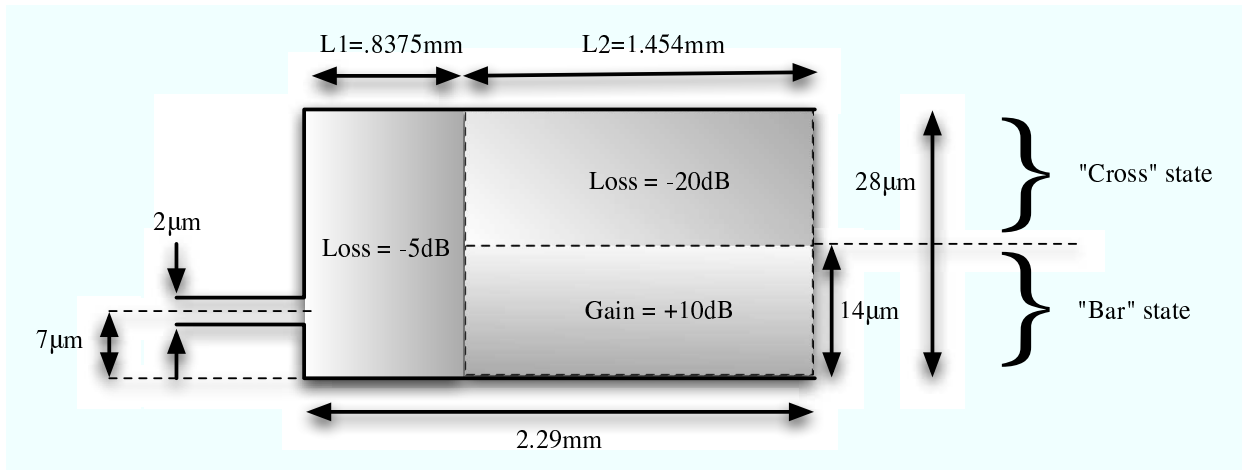


Figure 5.7: Schematic of a 3-segment PARMS with dimensions and values assigned.

In order to improve device design, the mechanism behind switching in these multimode devices needs to be analyzed – specifically, is the power switching induced by gain-dependent phase-shift or just amplitude modulation? To determine this, the device is re-simulated with no linewidth enhancement; therefore, any power switching can only be caused by “gain-guiding”. As figure 5.9 demonstrates, the thresholding abilities of this device are greatly reduced with no induced phase-shift resultant from the saturable active region.

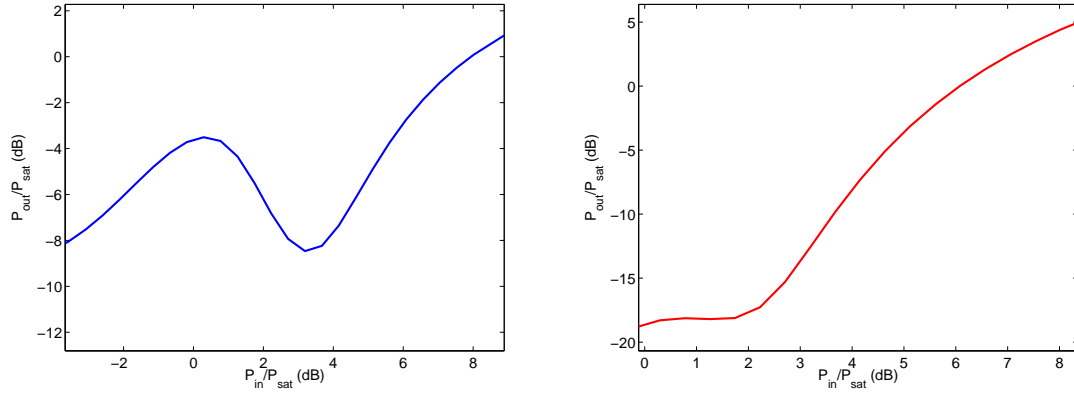


Figure 5.8: Output power from the two output waveguides of the PARMS shown in figure 5.8. The bar state output (left) and the cross state output (right) both demonstrate thresholding abilities.

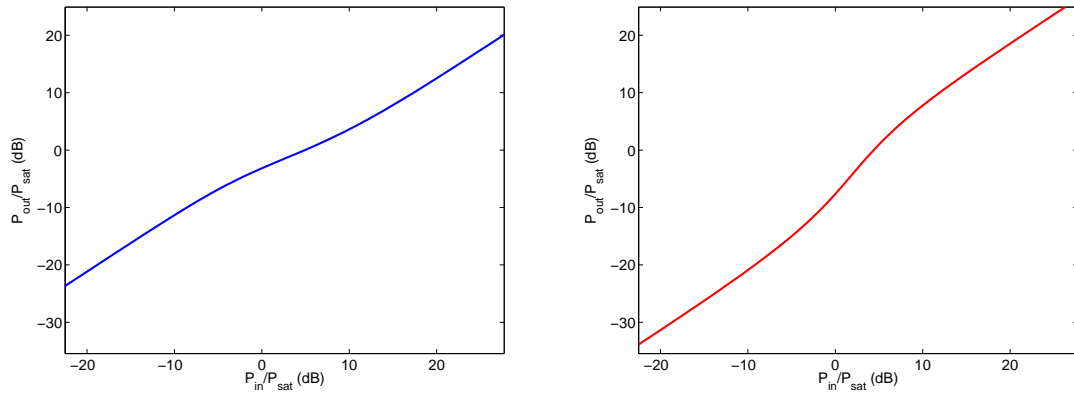


Figure 5.9: Output power from the two output waveguides of the PARMS shown in figure 5.8, but with no linewidth enhancement (intensity-dependent phase-shift). The bar state output (left) and the cross state output (right) both demonstrate greatly reduced thresholding capabilities as compared with figure 5.8 in which the Henry- α factor is 5.

Chapter 6

Conclusion and Future Work

In this work, the first evaluations of patterned active region multimode switches (PARMS) for use in optical thresholding are evaluated. Chapters 2 - 4 examined the fundamental theories behind PARMS operation and chapter 5 presented the first simulated results. The initial results demonstrate a definite ability (in theory) for a high extinction ratio thresholder PARMS, which has a larger extinction ratio over a smaller input power span than SOA-MMIs (in simulation) [7, 8]. These devices were designed with a pre-existing device “recipe” and the geometry and bias of the active regions were selected through basic simulation optimization. To further improve these devices and simulation accuracy, experimental validation needs to be performed and new software needs to be created to optimize the device design.

The simulated device in chapter 5 along with one other PARMS designs are currently being fabricated at a commercial fabrication plant, but at this time, they are incomplete. The mask-design for the device showcased in chapter 5, is shown in figure 6.1. The second PARMS mask, which also is $28\mu m$ wide, is shown in figure 6.2. This device contains 8 electrically isolated active regions and is approximately twice as long. Both of the fabricated PARMS designs contain two input waveguides, which are both $2\mu m$ wide and offset from the center of the device by $7\mu m$.

Experimentation of these devices will not only verify (or reject) the basic operational abilities of these devices, but will also produce the actual linewidth



Figure 6.1: Schematic of a 3-segment PARMS device in fabrication. The light-gray segments are the metal contacts and the black and dark-gray areas are the active waveguides (the dark-gray segments are the active waveguide with a layer of metal overtop).



Figure 6.2: Schematic of an 8-segment PARMS device in fabrication. The light-gray segments are the metal contacts and the black and dark-gray areas are the active waveguides (the dark-gray segments are the active waveguide with a layer of metal overtop).

enhancement factor value, saturation intensities, and maximum gain (or loss) values for the active regions so that more accurate simulations can be performed in the future.

The device design from chapter 5 and the closely related alternate design, which was also sent for fabrication, were designed with simple active region geometries that were chosen and optimized through basic trial-and-error, simulations, and intuition. To maximize the thresholding capabilities of a PARMS, further software needs to be created, which calculates performance while varying device length and width as well as active region shapes, size, number, and gain (or loss) values. This software would no-doubt be complicated and time-consuming, but it could possibly predict very powerful PARMS thresholders.

Additionally, tailoring the fabrication *recipe* for these device could enhance their operation. The current design formed a weakly guiding structure that lost

much of its energy to radiation and required a fairly wide waveguide for multimode support. A larger effective index contrast would reduce the waveguide width (to maintain the same number of supported, guided modes) and reduce the imaging length. Although the differential gain would have to dramatically increase to produce the same gain (P_{out}/P_{in}), the device could be scaled to sub-millimeter sizes with similar performance.

Appendix A

MATLAB Code: Solve for Guided Modes

The MATLAB function below solves for the longitudinal propagation constants, β , of the guided modes of a waveguide using the Newton-Raphson method.

```
%%%%%%%%%%%%%%%%%%%%%%%%%%%%%%%%%%%%%%%%%%%%%%%%%%%%%%%%%%%%%%%%%%%%%%%%%% %%%%%%%%%%
%%%%%%%%%%%%%%%%%%%%%%%%%%%%%%%%%%%%%%%%%%%%%%%%%%%%%%%%%%%%%%%%%%%%%%%%%%
%%%%%%%% function GuidedModesSolve
%%%%%%%%
%%%%%%%% Input:
%%%%%%%% n1,n2 – Core and cladding effective indices, respectively
%%%%%%%% lambda – Free-space wavelength of light
%%%%%%%% W_sm – Full-width of input waveguide
%%%%%%%% W_mmi – Full-width of multimode waveguide
%%%%%%%% W_box – Full-width of simulation window
%%%%%%%%
%%%%%%%% Output:
%%%%%%%% BetaGuideS, BetaGuideA – Longitudinal propagation
%%%%%%%% constants of the symmetric and asymmetric
%%%%%%%% guided modes (respectively) of the multimode
%%%%%%%% waveguide.
%%%%%%%% BetaSM – Longitudinal propagation constant corresponding
%%%%%%%% to the single supported input waveguide’s mode
%%%%%%%%
%%%%%%%%%%%%%%%%%%%%%%%%%%%%%%%%%%%%%%%%%%%%%%%%%%%%%%%%%%%%%%%%%%%%%%%%%% %%%%%%%%%%
```

```
function [BetaGuideS, BetaGuideA, BetaSM] = GuidedModesSolve(n1, n2, lambda,
W_sm, W_mmi, W_box)
```

```
%%%%%%%%%%%% Input Waveguide GUIDED Mode %%%%%%%%%%
```

```
k0 = (2*pi)/lambda; % Free-space propagation constant
```

```
k1 = k0.*n1; % Propagation constant in the core
```

```
k2 = n2.*k0; % Propagation constant in the cladding
```

```
%%%%%%%%%%%% "Guess" values for propagation constants %%%%%%%%%%
```

```
Beta = real(k2):real((k1-k2))/1e5:real(k1);
```

```
Gamma = sqrt(k1^2 - Beta.^2);
```

```
Alpha = sqrt(Beta.^2 - k2^2);
```

```
%%%%%%%%%%%%%% %%%%%%%%%%
```

```
%%%%%%%%%%%% Begin Newton-Raphson Method %%%%%%%%%%
```

```
F = ((Gamma./Alpha).*tan(Gamma.*(W_sm/2))) - ((1 +
exp(Alpha.*(W_sm-W_box)))/(1 - exp(Alpha.*(W_sm
-W_box))));
```

```
guess=[ ];
```

```
guess_count = 1;
```

```
%%%%%%%%%%%% Look for change in sign of F (rough estimate) %%%%%%%%%%
```

```

for counter = 1:length(Beta)-1
if(and(sign(F(counter)) > sign(F(counter+1)), isfinite(F(counter)) == 1))
guess(guess_count,1) = counter;
guess(guess_count,2) = Beta(counter);
guess(guess_count,3) = Beta(counter+1);
guess(guess_count,4) = F(counter);
guess_count = guess_count+1;
end
end

clear Beta;
clear Gamma;
clear Alpha;
clear F;
p_save = [ ];

%%%%%%%%%%%% Refine rough estimates %%%%%%%%%%%%%
for counter = 1:guess_count-1

p0 = guess(counter,2);
p1 = guess(counter,3);

for iter = 1:30
Gamma = sqrt(k1^2 - p0^2);
Alpha = sqrt(p0^2 - k2^2);
F = ((Gamma./Alpha).*tan(Gamma.*(W_sm/2))) - ((1 +

```

```

exp(Alpha.*(W_sm-W_box))./(1 - exp(Alpha.*(W_sm
-W_box))));

Gamma1 = sqrt(k1^2 - p1^2);
Alpha1 = sqrt(p1^2 - k2^2);
F1 = ((Gamma1./Alpha1).*tan(Gamma1.*(W_sm/2))) -
((1 + exp(Alpha1.*(W_sm- W_box))./(1 - exp(Alpha1.*(W_sm
-W_box))));

if(p1 == p0)
p_save(counter) = p0;
break;
end

F_prime = (F1 - F)/(p1-p0);

p = p0 - (F/F_prime);
p1 = p0;
p0 = p;

end
end

BetaSM = p_save(length(p_save));

clear Beta;
clear Gamma;
clear Alpha;

```

```

clear F;
clear p0;
clear p1;
clear p;
clear p_save;

%%%%%%%%%%%% End Newton-Raphson Method %%%%%%%%%%

%%%%%%%%%%%%%%

%%%%%%%%%%%% Multimode waveguide GUIDED Modes %%%%%%%%%%

% Symmetric Mode(s) %

k0 = (2*pi)/lambda;
k1 = k0.*n1;
k2 = n2.*k0;

Beta = k2:(k1-k2)/1e5:k1;
Gamma = sqrt(k1^2 - Beta.^2);
Alpha = sqrt(Beta.^2 - k2^2);

F = ((Gamma./Alpha).*tan(Gamma.*(W_mmi/2))) - ((1 +
exp(Alpha.*(W_mmi-W_box))./(1 - exp(Alpha.*(W_mmi
-W_box)))));

guess=[ ];

```



```

guess_count = 1;

for counter = 1:length(Beta)-1
if(and(sign(F(counter)) > sign(F(counter+1)), isfinite(F(counter)) == 1))
guess(guess_count,1) = counter;
guess(guess_count,2) = Beta(counter);
guess(guess_count,3) = Beta(counter+1);
guess(guess_count,4) = F(counter);
guess_count = guess_count+1;
end
end

clear Beta;
clear Gamma;
clear Alpha;
clear F;
p_save = [];

for counter = 1:guess_count-1

p0 = guess(counter,2);
p1 = guess(counter,3);

for iter = 1:20
Gamma = sqrt(k1^2 - p0^2);
Alpha = sqrt(p0^2 - k2^2);
F = ((Gamma./Alpha).*tan(Gamma.*(W_mmi/2))) - ((1 +

```

```

exp(Alpha.*(W_mmi-W_box))./(1 - exp(Alpha.*(W_mmi
-W_box))));

Gamma1 = sqrt(k1^2 - p1^2);
Alpha1 = sqrt(p1^2 - k2^2);
F1 = ((Gamma1./Alpha1).*tan(Gamma1.*(W_mmi/2))) - ((1 +
exp(Alpha1.*(W_mmi-W_box))./(1 - exp(Alpha1.*(W_mmi
-W_box))));

if(p1 == p0)
p_save(counter) = p0;
break;
end

F_prime = (F1 - F)/(p1-p0);

p = p0 - (F/F_prime);
p1 = p0;
p0 = p;

end
end

BetaGuideS = p_save;

clear Beta;
clear Gamma;
clear Alpha;

```

```

clear F;
clear p0;
clear p1;
clear p;
clear p_save;

%%%%%%%%%%%%%%%%%%%%%%%%%%%%%%%%%%%%%%%%%%%%%%%%%%%%%%%%%%%%%%%%%%%%%%%%

% Asymmetric Mode(s) %

Beta = k2:(k1-k2)/1e5:k1;
Gamma = sqrt(k1^2 - Beta.^2);
Alpha = sqrt(Beta.^2 - k2^2);

F = ((-Gamma./Alpha).*cot(Gamma.*(W_mmi/2))) - ((1 +
exp(Alpha.*(W_mmi-W_box))./(1 - exp(Alpha.*(W_mmi
-W_box)))));

guess=[ ];
guess_count = 1;

for counter = 1:length(Beta)-1
if(and(sign(F(counter)) > sign(F(counter+1)), isfinite(F(counter)) == 1))
guess(guess_count,1) = counter;
guess(guess_count,2) = Beta(counter);
guess(guess_count,3) = Beta(counter+1);
guess(guess_count,4) = F(counter);

```

```

guess_count = guess_count+1;
end
end

clear Beta;
clear Gamma;
clear Alpha;
clear F;
p_save = [ ];

for counter = 1:guess_count-1

p0 = guess(counter,2);
p1 = guess(counter,3);

for iter = 1:30
Gamma = sqrt(k1^2 - p0^2);
Alpha = sqrt(p0^2 - k2^2);
F = ((-Gamma./Alpha).*cot(Gamma.*(W_mmi/2))) - ((1 +
exp(Alpha.*(W_mmi-W_box))./(1 - exp(Alpha.*(W_mmi
-W_box))));

Gamma1 = sqrt(k1^2 - p1^2);
Alpha1 = sqrt(p1^2 - k2^2);
F1 = ((-Gamma1./Alpha1).*cot(Gamma1.*(W_mmi/2))) - ((1 +
exp(Alpha1.*(W_mmi-W_box))./(1 - exp(Alpha1.*(W_mmi
-W_box))));

```

```

if(p1 == p0)
p_save(counter) = p0;
break;
end

F_prime = (F1 - F)/(p1-p0);

p = p0 - (F/F_prime);
p1 = p0;
p0 = p;

end
end
BetaGuideA = p_save;

clear Beta;
clear Gamma;
clear Alpha;
clear F;
clear p0;
clear p1;
clear p;
clear p_save;

BetaGuideS = fliplr(unique((nonzeros(BetaGuideS))'));
BetaGuideA = fliplr(unique((nonzeros(BetaGuideA))'));

```


Appendix B

MATLAB Code: Solve for Radiative Modes

The MATLAB function below solves for the longitudinal propagation constants, β , of the radiative modes of a waveguide. The returned propagation constants are limited to the set, which obeys the virtual boundary condition (VBC) and will not reflect back into the system.

```
%%%%%%%%%%%%%%%%%%%%%%%%%%%%%%%%%%%%%%%%%%%%%%%%%%%%%%%%%%%%%%%%%%%%%%%%
%%%%%%%%%%%%%%%%%%%%%%%%%%%%%%%%%%%%%%%%%%%%%%%%%%%%%%%%%%%%%%%%
%%%%%%%%%%%%%%%%%%%%%%%%%%%%%%%%%%%%%%%%%%%%%%%%%%%%%%%%%%%%%%%%
%%%%%%%%%%%%%%%%%%%%%%%%%%%%%%%%%%%%%%%%%%%%%%%%%%%%%%%%%%%%%%%% function AllModesSolve_lim
%%%%%%%%%%%%%%%%%%%%%%%%%%%%%%%%%%%%%%%%%%%%%%%%%%%%%%%%%%%%%%%%
%%%%%%%%%%%%%%%%%%%%%%%%%%%%%%%%%%%%%%%%%%%%%%%%%%%%%%%%%%%%%%%% Input:
%%%%%%%%%%%%%%%%%%%%%%%%%%%%%%%%%%%%%%%%%%%%%%%%%%%%%%%%%%%%%%%% n1,n2 – Core and cladding effective indices, respectively
%%%%%%%%%%%%%%%%%%%%%%%%%%%%%%%%%%%%%%%%%%%%%%%%%%%%%%%%%%%%%%%% lambda – Free-space wavelength of light
%%%%%%%%%%%%%%%%%%%%%%%%%%%%%%%%%%%%%%%%%%%%%%%%%%%%%%%%%%%%%%%% W_sm – Full-width of input waveguide
%%%%%%%%%%%%%%%%%%%%%%%%%%%%%%%%%%%%%%%%%%%%%%%%%%%%%%%%%%%%%%%% W_mmi – Full-width of multimode waveguide
%%%%%%%%%%%%%%%%%%%%%%%%%%%%%%%%%%%%%%%%%%%%%%%%%%%%%%%%%%%%%%%% W_box – Full-width of virtual boundary condition (VBC)
%%%%%%%%%%%%%%%%%%%%%%%%%%%%%%%%%%%%%%%%%%%%%%%%%%%%%%%%%%%%%%%% L – Length of multimode waveguide
%%%%%%%%%%%%%%%%%%%%%%%%%%%%%%%%%%%%%%%%%%%%%%%%%%%%%%%%%%%%%%%% beta_num – number of “guess” betas
%%%%%%%%%%%%%%%%%%%%%%%%%%%%%%%%%%%%%%%%%%%%%%%%%%%%%%%%%%%%%%%%
%%%%%%%%%%%%%%%%%%%%%%%%%%%%%%%%%%%%%%%%%%%%%%%%%%%%%%%%%%%%%%%% Output:
%%%%%%%%%%%%%%%%%%%%%%%%%%%%%%%%%%%%%%%%%%%%%%%%%%%%%%%%%%%%%%%% BetaRadS, BetaRadA – Longitudinal propagation
%%%%%%%%%%%%%%%%%%%%%%%%%%%%%%%%%%%%%%%%%%%%%%%%%%%%%%%%%%%%%%%% constants of the symmetric and asymmetric
%%%%%%%%%%%%%%%%%%%%%%%%%%%%%%%%%%%%%%%%%%%%%%%%%%%%%%%%%%%%%%%% radiative modes (respectively) of the multimode
%%%%%%%%%%%%%%%%%%%%%%%%%%%%%%%%%%%%%%%%%%%%%%%%%%%%%%%%%%%%%%%% waveguide.
```

```

%%%%
%%%%%%%%%%%%%%%%%%%%%%%%%%%%%%%%%%%%%%%%%%%%%%%%%%%%%%%%%%%%%%%%%%%%%%%%

function [BetaRadS, BetaRadA] = AllModesSolve_lim(n1, n2, lambda, W_sm,
W_mmi, W_box, L, beta_num)

%%%%%%%%%%%%%%%%%%%%%%%%%%%%%%%%%%%%%%%%%%%%%%%%%%%%%%%%%%%%%%%%%%%%%%%%

%%%%%%%%%%%%%%%%%%%%%%%%%%%%%%%%%%%%%%%%%%%%%%%%%%%%%%%%%%%%%%%%%%%%%%%% MMI RADIATIVE MODES %%%%%%%%%

% Symmetric

%%%%%%%%%%%%%%%%%%%%%%%%%%%%%%%%%%%%%%%%%%%%%%%%%%%%%%%%%%%%%%%%%%%%%%%% Determine maximum propagation angle for VBC

xx = W_mmi/2;
yy = (W_box/2)-(W_mmi/2);
theta = atan((xx+2*yy)/L); % Max angle

%%%%%%%%%%%%%%%%%%%%%%%%%%%%%%%%%%%%%%%%%%%%%%%%%%%%%%%%%%%%%%%%%%%%%%%%

k0 = (2*pi)/lambda; % Free-space propagation constant
k2 = k0*n2; % Propagation constant in the cladding
k1 = n1*k0; % Propagation constant in the core

high_lim = k2; % Maximum Beta
low_lim = cos(theta)*k2; % Minimum Beta

```


%%%%%%%%%% “Guess” values for propagation constants %%%%%%%%%%

```
temp_beta = linspace(low_lim,high_lim,beta_num);
```

```
Beta = temp_beta(1:length(temp_beta)-1);
```

```
Gamma = sqrt(k1^2 - Beta.^2);
```

```
Alpha = sqrt(k2^2 - Beta.^2);
```

%%%%%%%%%%

%%%%%%%%%% Begin Newton-Raphson Method %%%%%%%%%%

```
F = ((Gamma./Alpha).*tan(Gamma.*(W_mmi/2))) - ((sin(Alpha.*(W_mmi./2)) +  
cot(Alpha.*(W_box/2)).*cos(Alpha.*(W_mmi/2)))./(cos(Alpha.*(W_mmi/2)) -  
cot(Alpha.*(W_box/2)).*sin(Alpha.*(W_mmi/2))));
```

```
guess=[];
```

```
guess_count = 1;
```

%%%%%%%%%% Look for change in sign of F (rough estimate) %%%%%%%%%%

```
for counter = 1:length(Beta)-1
```

```
if(and(sign(F(counter)) > sign(F(counter+1)), isfinite(F(counter)) == 1))
```

```
guess(guess_count,1) = counter;
```

```
guess(guess_count,2) = Beta(counter);
```

```
guess(guess_count,3) = Beta(counter+1);
```

```

guess(guess_count,4) = F(counter);
guess_count = guess_count+1;
end
end

clear Trans1;
clear Trans2;
clear Beta;
clear Gamma;
clear Alpha;
clear F;
p_save = [];

%%%%%%%%%% Refine rough estimates %%%%%%%%%%

for counter = 1:guess_count-1

p0 = guess(counter,2);
p1 = guess(counter,3);

for iter = 1:20
Gamma = sqrt(k1^2 - p0^2);
Alpha = sqrt(k2^2 - p0^2);
F = ((Gamma./Alpha).*tan(Gamma.*(W_mmi/2))) - ((sin(Alpha.*(W_mmi./2))
+ cot(Alpha.*(W_box/2)).*cos(Alpha.*(W_mmi/2)))./(cos(Alpha.*(W_mmi/2)) -
cot(Alpha.*(W_box/2)).*sin(Alpha.*(W_mmi/2))));

```

```

Gamma1 = sqrt(k1^2 - p1^2);
Alpha1 = sqrt(k2^2 - p1^2);
F1 = ((Gamma1./Alpha1).*tan(Gamma1.*(W_mmi/2))) - ((sin(Alpha1.*(W_mmi./2))+
cot(Alpha1.*(W_box/2)).*cos(Alpha1.*(W_mmi/2)))./
(cos(Alpha1.*(W_mmi/2))- cot(Alpha1.*(W_box/2)).*sin(Alpha1.*(W_mmi/2))));

    if(p1 == p0)
if (p0 > 0)
p_save(counter) = p0;
end
break;
end

F_prime = (F1 - F)/(p1-p0);

p = p0 - (F/F_prime);
p1 = p0;
p0 = p;

end
end
BetaRadS = p_save;

clear Beta;
clear Gamma;
clear Alpha;
clear F;

```

```

clear p0;
clear p1;
clear p;
clear p_save;

%%%%%%%%%%%% End Newton-Raphson Method %%%%%%%%%%

%%%%%%%%%%%%

% Asymmetric

%%%%%%%%%%%% “Guess” values for propagation constants %%%%%%%%%%

Beta = temp_beta(1:length(temp_beta)-1);
Gamma = sqrt(k1^2 - Beta.^2);
Alpha = sqrt(k2^2 - Beta.^2);

%%%%%%%%%%%%

%%%%%%%%%%%% Begin Newton-Raphson Method %%%%%%%%%%

F = ((-Gamma./Alpha).*cot(Gamma.*(W_mmi/2))) - ((sin(Alpha.*(W_mmi./2))
+ cot(Alpha.*(W_box/2)).*cos(Alpha.*(W_mmi/2)))./(cos(Alpha.*(W_mmi/2))
- cot(Alpha.*(W_box/2)).*sin(Alpha.*(W_mmi/2))));

guess=[];
guess_count = 1;

```

```

for counter = 1:length(Beta)-1
if(and(sign(F(counter)) > sign(F(counter+1)), isfinite(F(counter)) == 1))
guess(guess_count,1) = counter;
guess(guess_count,2) = Beta(counter);
guess(guess_count,3) = Beta(counter+1);
guess(guess_count,4) = F(counter);
guess_count = guess_count+1;
end
end

```

```
clear Beta;
```

```
clear Gamma;
```

```
clear Alpha;
```

```
clear F;
```

```
p_save = [];
```

```
%%%%%%%%%% Refine rough estimates %%%%%%%%%%
```

```
for counter = 1:guess_count-1
```

```
p0 = guess(counter,2);
```

```
p1 = guess(counter,3);
```

```
for iter = 1:20
```

```
Gamma = sqrt(k1^2 - p0^2);
```

```
Alpha = sqrt(k2^2 - p0^2);
```

```

F = ((-Gamma./Alpha).*cot(Gamma.*(W_mmi/2))) - ((sin(Alpha.*(W_mmi./2))
+ cot(Alpha.*(W_box/2)).*cos(Alpha.*(W_mmi/2)))./(cos(Alpha.*(W_mmi/2))
- cot(Alpha.*(W_box/2)).*sin(Alpha.*(W_mmi/2))));

```

```

Gamma1 = sqrt(k1^2 - p1^2);

```

```

Alpha1 = sqrt(k2^2 - p1^2);

```

```

F1 = ((-Gamma1./Alpha1).*cot(Gamma1.*(W_mmi/2))) - ((sin(Alpha1.*
(W_mmi./2)) + cot(Alpha1.*(W_box/2)).*cos(Alpha1.*(W_mmi/2)))./
(cos(Alpha1.*(W_mmi/2)) - cot(Alpha1.*(W_box/2)).*sin(Alpha1.*
(W_mmi/2))));

```

```

if(p1 == p0)

```

```

    p_save(counter) = p0;

```

```

    break;

```

```

end

```

```

F_prime = (F1 - F)/(p1-p0);

```

```

p = p0 - (F/F_prime);

```

```

p1 = p0;

```

```

p0 = p;

```

```

end

```

```

end

```

```

BetaRadA = p_save;

```

```

%%%%%%%%%% End Newton-Raphson Method %%%%%%%%%%%

```

%%%

BetaRadS = fliplr(unique((nonzeros(BetaRadS))'));

BetaRadA = fliplr(unique((nonzeros(BetaRadA))'));

Appendix C

MATLAB: Dual-Waveguide Mode Solutions

The following MATLAB function solves for the longitudinal propagation constants (guided modes only) for two parallel waveguide.

```
%%%%%%%%%%%%%%%%%%%%%%%%%%%%%%%%%%%%%%%%%%%%%%%%%%%%%%%%%%%%%%%%%%%%%%%%%
```

```
%%%%%%%%%
```

```
%%%%%%%%% function ModeSolveDual
```

```
%%%%%%%%%
```

```
%%%%%%%%% Input:
```

```
%%%%%%%%% n1,n2 – Core and cladding effective indices, respectively
```

```
%%%%%%%%% lambda – Free-space wavelength of light
```

```
%%%%%%%%% W_sm – Full-width of each waveguide
```

```
%%%%%%%%% x1 – offset of the edge of waveguides from center of simulation window
```

```
%%%%%%%%% d – half-width of multimode waveguide
```

```
%%%%%%%%% L – Waveguides' length
```

```
%%%%%%%%%
```

```
%%%%%%%%% Output:
```

```
%%%%%%%%% BetaGuideSym, BetaGuideASym – Longitudinal propagation
```

```
%%%%%%%%% constants of the symmetric and asymmetric
```

```
%%%%%%%%% guided modes (respectively) of the multimode
```

```
%%%%%%%%% waveguide.
```

```
%%%%%%%%%
```

```
%%%%%%%%%%%%%%%%%%%%%%%%%%%%%%%%%%%%%%%%%%%%%%%%%%%%%%%%%%%%%%%%%%%%%%%%%
```



```
function [BetaGuideSym,BetaGuideASym] = ModeSolveDual(n1, n2, lambda, W_sm,
x1, d, L)
```

```
    k0 = (2*pi)/lambda; % Free-space propagation constant
```

```
    k1 = k0.*n1; % Propagation constant in the core
```

```
    k2 = n2.*k0; % Propagation constant in the cladding
```

```
    %%%%%%%%%%% “Guess” values for propagation constants %%%%%%%%%%%
```

```
    Beta_min = k2*cos(atan(d/L));
```

```
    Beta = k2:(k1-k2)/1e6:k1;
```

```
    Gamma = sqrt(k1^2 - Beta.^2);
```

```
    Alpha = sqrt(Beta.^2 - k2^2);
```

```
    %%%%%%%%%%%
```

```
    %%%%%%%%%%% Begin Newton-Raphson Method %%%%%%%%%%%
```

```
    % Symmetric
```

```
    B = sinh(Alpha.*x1).*cos(Gamma.*x1) - (Alpha./Gamma).*cosh(Alpha.*x1).*
    sin(Gamma.*x1);
```

```
    C = (sinh(Alpha.*x1) - B.*cos(Gamma.*x1))./sin(Gamma.*x1);
```

```
    Left_side = (Gamma./Alpha).*tanh(Alpha.*(x1+W_sm-d));
```

```

Right_side = (B.*cos(Gamma.*(x1+W_sm)) + C.*sin(Gamma.*(x1+W_sm)))./
(-B.*sin(Gamma.*(x1+W_sm)) + C.*cos(Gamma.*(x1+W_sm)));
F = -Left_side + Right_side;

```

```

guess=[];

```

```

guess_count = 1;

```

```

%%%%%%%%%% Look for change in sign of F (rough estimate) %%%%%%%%%%

```

```

for counter = 1:length(Beta)-1

```

```

if(and(sign(F(counter)) > sign(F(counter+1)), isfinite(F(counter)) == 1))

```

```

guess(guess_count,1) = counter;

```

```

guess(guess_count,2) = Beta(counter);

```

```

guess(guess_count,3) = Beta(counter+1);

```

```

guess(guess_count,4) = F(counter);

```

```

guess_count = guess_count+1;

```

```

end

```

```

end

```

```

clear Beta;

```

```

clear Gamma;

```

```

clear Alpha;

```

```

clear F;

```

```

clear B;

```

```

clear C;

```

```

p_save = [];

```

```

%%%%%%%%%% Refine rough estimates %%%%%%%%%%

for counter = 1:guess_count-1

p0 = guess(counter,2);
p1 = guess(counter,3);

for iter = 1:10
Gamma = sqrt(k1^2 - p0^2);
Alpha = sqrt(p0^2 - k2^2);
B = sinh(Alpha.*x1).*cos(Gamma.*x1) - (Alpha./Gamma).*cosh(Alpha.*x1).*
sin(Gamma.*x1);

C = (sinh(Alpha.*x1) - B.*cos(Gamma.*x1))./sin(Gamma.*x1);

Left_side = (Gamma./Alpha).*tanh(Alpha.*(x1+W_sm-d));

Right_side = (B.*cos(Gamma.*(x1+W_sm)) + C.*sin(Gamma.*(x1+W_sm)))./
(-B.*sin(Gamma.*(x1+W_sm)) + C.*cos(Gamma.*(x1+W_sm)));

F = -Left_side + Right_side;

Gamma1 = sqrt(k1^2 - p1^2);
Alpha1 = sqrt(p1^2 - k2^2);
B1 = sinh(Alpha1.*x1).*cos(Gamma1.*x1) - (Alpha1./Gamma1).*
cosh(Alpha1.*x1).*sin(Gamma1.*x1);

```

```
C1 = (sinh(Alpha1.*x1) - B1.*cos(Gamma1.*x1))./sin(Gamma1.*x1);
```

```
Left_side1 = (Gamma1./Alpha1).*tanh(Alpha1.*(x1+W_sm-d));
```

```
Right_side1 = (B1.*cos(Gamma1.*(x1+W_sm)) + C1.*sin(Gamma1.*(x1+W_sm)))./  
(-B1.*sin(Gamma1.*(x1+W_sm)) + C1.*cos(Gamma1.*(x1+W_sm)));
```

```
F1 = -Left_side1 + Right_side1;
```

```
if(p1 == p0)
```

```
    p_save(counter) = p0;
```

```
    break;
```

```
end
```

```
F_prime = (F1 - F)/(p1-p0);
```

```
p = p0 - (F/F_prime);
```

```
p1 = p0;
```

```
p0 = p;
```

```
end
```

```
end
```

```
BetaGuideASym = p_save;
```

```
clear Beta;
```

```

clear Gamma;
clear Alpha;
clear F;
clear B;
clear C;
clear Beta1;
clear Gamma1;
clear Alpha1;
clear F1;
clear B1;
clear C1;

%%%%%%%%%%%% End Newton-Raphson Method %%%%%%%%%%

%%%%%%%%%%%%%

% Asymmetric

Beta = k2:(k1-k2)/1e6:k1;
Gamma = sqrt(k1^2 - Beta.^2);
Alpha = sqrt(Beta.^2 - k2^2);

B = cosh(Alpha.*x1).*cos(Gamma.*x1) - (Alpha./Gamma).*sinh(Alpha.*x1).*
sin(Gamma.*x1);

C = (cosh(Alpha.*x1) - B.*cos(Gamma.*x1))./sin(Gamma.*x1);

```

```
Left_side = (Gamma./Alpha).*tanh(Alpha.*(x1+W_sm-d));
```

```
Right_side = (B.*cos(Gamma.*(x1+W_sm)) + C.*sin(Gamma.*(x1+W_sm)))./  
(-B.*sin(Gamma.*(x1+W_sm)) + C.*cos(Gamma.*(x1+W_sm)));
```

```
F = -Left_side + Right_side;
```

```
guess=[];
```

```
guess_count = 1;
```

```
for counter = 1:length(Beta)-1
```

```
if(and(sign(F(counter)) > sign(F(counter+1)), isfinite(F(counter)) == 1))
```

```
guess(guess_count,1) = counter;
```

```
guess(guess_count,2) = Beta(counter);
```

```
guess(guess_count,3) = Beta(counter+1);
```

```
guess(guess_count,4) = F(counter);
```

```
guess_count = guess_count+1;
```

```
end
```

```
end
```

```
clear Beta;
```

```
clear Gamma;
```

```
clear Alpha;
```

```
clear F;
```

```
clear B;
```

```
clear C;
```

```

p_save = [];

for counter = 1:guess_count-1

p0 = guess(counter,2);
p1 = guess(counter,3);

for iter = 1:10
Gamma = sqrt(k1^2 - p0^2);
Alpha = sqrt(p0^2 - k2^2);

B = cosh(Alpha.*x1).*cos(Gamma.*x1) - (Alpha./Gamma).*sinh(Alpha.*x1).*
sin(Gamma.*x1);

C = (cosh(Alpha.*x1) - B.*cos(Gamma.*x1))./sin(Gamma.*x1);

Left_side = (Gamma./Alpha).*tanh(Alpha.*(x1+W_sm-d));

Right_side = (B.*cos(Gamma.*(x1+W_sm)) + C.*sin(Gamma.*(x1+W_sm)))./
(-B.*sin(Gamma.*(x1+W_sm)) + C.*cos(Gamma.*(x1+W_sm)));

F = -Left_side + Right_side;

Gamma1 = sqrt(k1^2 - p1^2);
Alpha1 = sqrt(p1^2 - k2^2);

```

```
B1 = cosh(Alpha1.*x1).*cos(Gamma1.*x1) - (Alpha1./Gamma1).*  
sinh(Alpha1.*x1).*sin(Gamma1.*x1);
```

```
C1 = (cosh(Alpha1.*x1) - B1.*cos(Gamma1.*x1))./sin(Gamma1.*x1);
```

```
Left_side1 = (Gamma1./Alpha1).*tanh(Alpha1.*(x1+W_sm-d));
```

```
Right_side1 = (B1.*cos(Gamma1.*(x1+W_sm)) + C1.*sin(Gamma1.*  
(x1+W_sm)))./(-B1.*sin(Gamma1.*(x1+W_sm)) + C1.*cos(Gamma1.*  
(x1+W_sm)));
```

```
F1 = -Left_side1 + Right_side1;
```

```
if(p1 == p0)
```

```
    p_save(counter) = p0;
```

```
    break;
```

```
end
```

```
F_prime = (F1 - F)/(p1-p0);
```

```
p = p0 - (F/F_prime);
```

```
p1 = p0;
```

```
p0 = p;
```

```
end
```

```
end
```

```
BetaGuideSym = p_save;
```



```
BetaGuideSym = fliplr(unique((nonzeros(BetaGuideSym))'));)
```

```
BetaGuideASym = fliplr(unique((nonzeros(BetaGuideASym))'));
```

Appendix D

MATLAB: Modal Propagation Analysis of Guided Modes through Dual-Waveguides

This MATLAB function solves for the propagation constants corresponding to the guided super-modes of a dual waveguide set.

```
%%%%%%%%%%%%%%%%%%%%%%%%%%%%%%%%%%%%%%%%%%%%%%%%%%%%%%%%%%%%%%%%%%%%%%%%%%  
%%%%%%%%%%%%%%%%%%%%%%%%%%%%%%%%%%%%%%%%%%%%%%%%%%%%%%%%%%%%%%%%%%%%%%%%%%  
%%%%%%%%%%%%%%%%%%%%%%%%%%%%%%%%%%%%%%%%%%%%%%%%%%%%%%%%%%%%%%%%%%%%%%%%%%  
function DualGuides  
%%%%%%%%%%%%%%%%%%%%%%%%%%%%%%%%%%%%%%%%%%%%%%%%%%%%%%%%%%%%%%%%%%%%%%%%%%  
%%%%%%%%%%%%%%%%%%%%%%%%%%%%%%%%%%%%%%%%%%%%%%%%%%%%%%%%%%%%%%%%%%%%%%%%%%  
Input:  
%%%%%%%%%%%%%%%%%%%%%%%%%%%%%%%%%%%%%%%%%%%%%%%%%%%%%%%%%%%%%%%%%%%%%%%%%%  
n1,n2 – Core and cladding effective indices, respectively  
lambda – Free-space wavelength of light  
a – Full-width of each waveguide  
x1 – offset of the edge of waveguides from center of simulation window  
d – half-width of multimode waveguide  
E_sm – E-field incident to dual waveguides  
dx – lateral direction discretization width  
dz – longitudinal direction discretization width  
L – Waveguides' length  
%%%%%%%%%%%%%%%%%%%%%%%%%%%%%%%%%%%%%%%%%%%%%%%%%%%%%%%%%%%%%%%%%%%%%%%%%%  
Output:  
%%%%%%%%%%%%%%%%%%%%%%%%%%%%%%%%%%%%%%%%%%%%%%%%%%%%%%%%%%%%%%%%%%%%%%%%%%  
index – matrix representing indices of refraction  
E_out – Resulting output E-field  
zsteps – number of dz steps taken
```

```

%%%%
%%%%%%%%%%%%%%%%%%%%%%%%%%%%%%%%%%%%%%%%%%%%%%%%%%%%%%%%%%%%%%%%%%%%%%%%
function [index,E_out,zsteps] = DualGuides(n1,n2,lambda,a,x1,d,E_sm,dx,dz,L)

k0 = (2*pi)/lambda; % Free-space propagation constant
k1 = n1*k0; % Propagation constant in the core
k2 = n2*k0; % Propagation constant in the cladding

% Find the Guided-mode betas for dual waveguides
[BetaGuideSym , BetaGuideASym] = ModeSolveDual(n1, n2, lambda, a, x1, d, L);

GammaGuideSym = sqrt(k1^2 - BetaGuideSym.^2);
AlphaGuideSym = sqrt(BetaGuideSym.^2 - k2^2);
GammaGuideASym = sqrt(k1^2 - BetaGuideASym.^2);
AlphaGuideASym = sqrt(BetaGuideASym.^2 - k2^2);

x_3 = -x1:dx:x1;
x_4 = x1+dx:dx:x1+a;
x_5 = x1+a+dx:dx:d;
x_2 = -x1-a:dx:-x1-dx;
x_1 = -d:dx:-x1-a-dx;

x = [x_1 x_2 x_3 x_4 x_5];
x = unique(x);

PhiS = zeros(length(BetaGuideSym),length(x));
PhiA = zeros(length(BetaGuideASym),length(x));

```

```
%%%% Symmetric Mode Shapes %%%%
```

```
for counter = 1:length(BetaGuideSym)
```

```
B = cosh(AlphaGuideSym(counter).*x1).*cos(GammaGuideSym(counter).*x1) -  
(AlphaGuideSym(counter)./GammaGuideSym(counter)).*  
sinh(AlphaGuideSym(counter).*x1).*sin(GammaGuideSym(counter).*x1);
```

```
C = (cosh(AlphaGuideSym(counter).*x1) - B.*cos(GammaGuideSym(counter).* x1))./sin(Gamma
```

```
A = (B.*cos(GammaGuideSym(counter).*(x1+a)) + C.*sin(GammaGuideSym(counter).*(x1+a)))  
(x1+a-d));
```

```
Phi3S = cosh(AlphaGuideSym(counter).*x_3);
```

```
Phi4S = B.*cos(GammaGuideSym(counter).*x_4) +  
C.*sin(GammaGuideSym(counter).*x_4);
```

```
Phi5S = A.*sinh(AlphaGuideSym(counter).*(x_5-d));
```

```
Phi2S = fliplr(Phi4S);
```

```
Phi1S = fliplr(Phi5S);
```

```
PhiS(counter,:) = [Phi1S Phi2S Phi3S Phi4S Phi5S];
```

```
PhiS(counter,:) = (1/sqrt(trapz(x,PhiS(counter,:).^2)).*PhiS(counter,:);
```

```
end
```

%%%% Asymmetric Mode Shapes %%%%

```
for counter = 1:length(BetaGuideASym)
B = sinh(AlphaGuideASym(counter).*x1).*cos(GammaGuideASym(counter).*x1)
- (AlphaGuideASym(counter)./GammaGuideASym(counter)).*
cosh(AlphaGuideASym(counter).*x1).*sin(GammaGuideASym(counter).*x1);

C = (sinh(AlphaGuideASym(counter).*x1) -
B.*cos(GammaGuideASym(counter).*x1))./sin(GammaGuideASym(counter).*
x1);

A = (B.*cos(GammaGuideASym(counter).*(x1+a)) +
C.*sin(GammaGuideASym(counter).*(x1+a)))./
sinh(AlphaGuideASym(counter).*(x1+a-d));

Phi3A = sinh(AlphaGuideASym(counter).*x_3);
Phi4A = B.*cos(GammaGuideASym(counter).*x_4) + C.*
sin(GammaGuideASym(counter).*x_4);

Phi5A = A.*sinh(AlphaGuideASym(counter).*(x_5-d));
Phi2A = fliplr(-1.*Phi4A);
Phi1A = fliplr(-1.*Phi5A);

PhiA(counter,:) = [Phi1A Phi2A Phi3A Phi4A Phi5A];
PhiA(counter,:) = (1/sqrt(trapz(x,PhiA(counter,:).^2))).*PhiA(counter,:);
end
```

```

z = 0:dz:L;
zsteps = length(z);
xsteps = length(x);

index = zeros(xsteps,zsteps);
Absorp = index;

for counter = 1:xsteps
if(abs(x(counter)) >= x1+a+dx)
index(counter,:) = n2;
Absorp(counter,:) = 200;
elseif(abs(x(counter)) <= x1)
index(counter,:) = n2;
Absorp(counter,:) = 200;
else
index(counter,:) = n1;
Absorp(counter,:) = 0;
end
end

cS = zeros(length(BetaGuideSym), zsteps);
cA = zeros(length(BetaGuideASym), zsteps);

E_out = zeros(xsteps,zsteps);
I_out = E_out;

```

```

for counter = 1:length(GammaGuideSym)
cS(counter,1) = trapz(x,E_sm.*conj(PhiS(counter,:)));
E_out(:,1) = E_out(:,1) + (cS(counter,1).*PhiS(counter,:))';
end

```

```

for counter = 1:length(GammaGuideASym)
cA(counter,1) = trapz(x,E_sm.*conj(PhiA(counter,:)));
E_out(:,1) = E_out(:,1) + (cA(counter,1).*PhiA(counter,:))';
end

```

```

for countz = 2:zsteps
for counter = 1:length(GammaGuideSym)
E_out(:,countz) = E_out(:,countz) + (cS(counter,countz-1).*PhiS(counter,:).*
exp(j.*(BetaGuideSym(1) - BetaGuideSym(counter)).*z(countz))))';
end

```

```

for counter = 1:length(GammaGuideASym)
E_out(:,countz) = E_out(:,countz) + (cA(counter,countz-1).*PhiA(counter,:).*
exp(j.*(BetaGuideSym(1) - BetaGuideASym(counter)).*z(countz))))';
end

```

```

for counter = 1:length(GammaGuideSym)
cS(counter, countz) = (trapz(x,E_out(:,countz).*conj(PhiS(counter,:).*
exp(j*(BetaGuideSym(1)-BetaGuideSym(counter)).*z(countz))))');
end

```

```

for counter = 1:length(GammaGuideASym)

```

```
cA(counter, countz) = (trapz(x,E_out(:,countz).*conj(PhiA(counter,:)).*  
exp(j*(BetaGuideSym(1)-BetaGuideASym(counter)).*z(countz)))));  
end  
end
```


Appendix E

MATLAB Code: Modal Propagation Analysis (MPA) with Radiative Modes and Patterned Active Regions

The following MATLAB script simulates light propagating through a patterned active region multimode switch (PARMS). The light enters the PARMS through a single input and exits via twin output waveguides. This script utilizes the function found in Appendices A-D.

```
clear
```

```
n1 = 3.285; % Index of refraction in the core
```

```
n2 = 3.2833; % Index of refraction in the cladding
```

```
lambda = 1550e-9; % Free-space wavelength
```

```
k0 = (2*pi)/lambda; % Free-space propagation constant
```

```
k1 = n1*k0; % Propagation constant in the core
```

```
k2 = n2*k0; % Propagation constant in the cladding
```

```
W_mmi = 28e-6; % Full-width of multimode waveguide
```

```
W_box = 60e-6; % Full-width of simulation window
```

```
W_box2 = 400e-6; % Full-width of virtual boundary condition (VBC)
```

```
W_sm = 2e-6; % Full-width of single-mode input waveguide
```

```
dx = .1e-7; % Lateral direction discretization width
```

```

dz = 35e-6; % Propagation direction discretization length

offset = -W_mmi/4 - W_sm/2; % Offset of single-mode input waveguide – in this
% case centered between the middle and the edge

alpha = 5; % Linewidth enhancement factor

E_amp = .005; % Electric field peak amplitude

%%%% Find Betas of the Guided Modes %%%%

[BetaGuideS, BetaGuideA, BetaSM] = GuidedModesSolve(n1, n2, lambda, W_sm,
W_mmi, W_box);

%%%% Find Betas of Radiative Modes with VBC %%%%

[BetaRadS, BetaRadA] = AllModesSolve_lim(n1, n2, lambda, W_sm, W_mmi,
W_box2, L, 100000);

%%%% Corresponding Gamma's and Alpha's %%%%

GammaSM = sqrt(k1^2 - BetaSM.^2);
GammaGuideS = sqrt(k1^2 - BetaGuideS.^2);
GammaGuideA = sqrt(k1^2 - BetaGuideA.^2);
AlphaGuideS = sqrt(BetaGuideS.^2 - k2^2);
AlphaGuideA = sqrt(BetaGuideA.^2 - k2^2);

GammaRadS = sqrt(k1^2 - BetaRadS.^2);
GammaRadA = sqrt(k1^2 - BetaRadA.^2);

```

```

AlphaRadS = sqrt(k2^2 - BetaRadS.^2)';
AlphaRadA = sqrt(k2^2 - BetaRadA.^2)';

%%%%%% Lateral-direction vector

% Simulation Window
x1 = -W_box/2:dx:(-W_mmi/2)-dx;
x2 = -W_mmi/2:dx:W_mmi/2;
x3 = (W_mmi/2)+dx:dx:W_box/2;
x = [x1 x2 x3];

% Virtual boundary condition (VBC)
x1_2 = -W_box2/2:dx:(-W_mmi/2)-dx;
x3_2 = (W_mmi/2)+dx:dx:W_box2/2;
x_temp = [x1_2 x2 x3_2];

%%%%%%%%%%%%%%%%%%%%%%%%%%%%%%%%%%%%%%%%%%%%%%%%%%%%%%%%

%%%%%% Individual Mode-shape Vectors
Sym_1 = zeros(length(GammaGuideS),length(x1));
Sym_2 = zeros(length(GammaGuideS),length(x2));
Sym_3 = zeros(length(GammaGuideS),length(x3));
Sym = zeros(length(GammaGuideS),length(x));

Asym_1 = zeros(length(GammaGuideA),length(x1));
Asym_2 = zeros(length(GammaGuideA),length(x2));
Asym_3 = zeros(length(GammaGuideA),length(x3));

```

```

Asym = zeros(length(GammaGuideA),length(x));

RSym_1 = zeros(length(GammaRadS),length(x1));
RSym_2 = zeros(length(GammaRadS),length(x2));
RSym_3 = zeros(length(GammaRadS),length(x3));
RSym = zeros(length(GammaRadS),length(x));

RAsym_1 = zeros(length(GammaRadA),length(x1));
RAsym_2 = zeros(length(GammaRadA),length(x2));
RAsym_3 = zeros(length(GammaRadA),length(x3));
RAsym = zeros(length(GammaRadA),length(x));

A = 1; % Modal Peak Amplitude (arbitrary – modes are normalized later)

%%%%%% Define Mode Shapes
% Symmetric, Guided

for counter = 1:length(GammaGuideS)
Sym_1(counter,:) = ((A.*cos(GammaGuideS(counter).*(W_mmi/2)))./
(exp(AlphaGuideS(counter).*(W_mmi/2)) - exp(-AlphaGuideS(counter).*
((W_mmi/2)-W_box))))).*(exp(-AlphaGuideS(counter).*x1) -
exp(AlphaGuideS(counter).*(x1+W_box)));

Sym_2(counter,:) = A.*cos(GammaGuideS(counter).*x2);

Sym_3(counter,:) = ((A.*cos(GammaGuideS(counter).*(W_mmi/2)))./
(exp(-AlphaGuideS(counter).*(W_mmi/2)) - exp(AlphaGuideS(counter).*

```

```

((W_mmi/2)-W_box))).*(exp(-AlphaGuideS(counter).*x3) -
exp(AlphaGuideS(counter).(x3-W_box)));

Sym(counter,:) = [Sym_1(counter,:) Sym_2(counter,:) Sym_3(counter,:)];

% Normalize
Sym(counter,:) = (1/sqrt(trapz(x,Sym(counter,).^2))).*Sym(counter,:);
end

% Asymmetric, Guided
for counter = 1:length(GammaGuideA)
Asym_1(counter,:) = ((A.*sin(GammaGuideA(counter).(W_mmi/2)))./
(exp(AlphaGuideA(counter).(W_mmi/2)) - exp(-AlphaGuideA(counter).*(
((W_mmi/2)-W_box))).*(exp(-AlphaGuideA(counter).*x1) -
exp(AlphaGuideA(counter).(x1+W_box))));

Asym_2(counter,:) = -A.*sin(GammaGuideA(counter).*x2);

Asym_3(counter,:) = ((-A.*sin(GammaGuideA(counter).(W_mmi/2)))./
(exp(-AlphaGuideA(counter).(W_mmi/2)) - exp(AlphaGuideA(counter).*(
((W_mmi/2)-W_box))).*(exp(-AlphaGuideA(counter).*x3) -
exp(AlphaGuideA(counter).(x3-W_box))));

Asym(counter,:) = [Asym_1(counter,:) Asym_2(counter,:) Asym_3(counter,:)];

%Normalize
Asym(counter,:) = (1/sqrt(trapz(x,Asym(counter,).^2))).*Asym(counter,:);

```

end

% Symmetric, Radiative

for counter = 1:length(GammaRadS)

% VBC

RSym_1_temp(counter,:) = ((A.*cos(GammaRadS(counter).*(W_mmi/2)))./
(cos(AlphaRadS(counter).*(W_mmi/2))-cot(AlphaRadS(counter).*(W_box2/2)).*
sin(AlphaRadS(counter).*(W_mmi/2))))).*(cos(AlphaRadS(counter).*x1_2) +
cot(AlphaRadS(counter).*(W_box2/2)).*sin(AlphaRadS(counter).*x1_2));

RSym_2_temp(counter,:) = A.*cos(GammaRadS(counter).*x2);

RSym_3_temp(counter,:) = ((A.*cos(GammaRadS(counter).*(W_mmi/2)))./
(cos(AlphaRadS(counter).*(W_mmi/2))-cot(AlphaRadS(counter).*(W_box2/2)).*
sin(AlphaRadS(counter).*(W_mmi/2))))).*(cos(AlphaRadS(counter).*x3_2) -
cot(AlphaRadS(counter).*(W_box2/2)).*sin(AlphaRadS(counter).*x3_2));

RSym_temp(counter,:) = [RSym_1_temp(counter,:) RSym_2_temp(counter,:) RSym_3_temp(counter,:)];

%Normalize

RSym_temp2(counter,:) = (1/sqrt(trapz(x_temp,RSym_temp(counter,:).^2))).*

RSym_temp(counter,:);

% Inside actual boundary window

RSym_1(counter,:) = ((A.*cos(GammaRadS(counter).*(W_mmi/2)))./

```
(cos(AlphaRadS(counter).*(W_mmi/2))-cot(AlphaRadS(counter).*(W_box2/2)).*
sin(AlphaRadS(counter).*(W_mmi/2))).*(cos(AlphaRadS(counter).*x1) +
cot(AlphaRadS(counter).*(W_box2/2)).*sin(AlphaRadS(counter).*x1));
```

```
RSym_2 = RSym_2_temp;
```

```
RSym_3(counter,:) = ((A.*cos(GammaRadS(counter).*(W_mmi/2)))./
(cos(AlphaRadS(counter).*(W_mmi/2))-cot(AlphaRadS(counter).*(W_box2/2)).*
sin(AlphaRadS(counter).*(W_mmi/2))).*(cos(AlphaRadS(counter).*x3) -
cot(AlphaRadS(counter).*(W_box2/2)).*sin(AlphaRadS(counter).*x3));
```

```
RSym(counter,:) = [RSym_1(counter,:) RSym_2(counter,:) RSym_3(counter,:)];
```

```
%Normalize
```

```
RSym(counter,:) = (1/sqrt(trapz(x_temp,RSym_temp(counter,:).^2))).*
```

```
RSym(counter,:);
```

```
end
```

```
% Asymmetric, Radiative
```

```
for counter = 1:length(GammaRadA)
```

```
% VBC
```

```
RAsym_1_temp(counter,:) = ((A.*sin(GammaRadA(counter).*(W_mmi/2)))./
(cos(AlphaRadA(counter).*(W_mmi/2))-cot(AlphaRadA(counter).*(W_box2/2)).*
sin(AlphaRadA(counter).*(W_mmi/2))).*(cos(AlphaRadA(counter).*x1_2) +
cot(AlphaRadA(counter).*(W_box2/2)).*sin(AlphaRadA(counter).*x1_2));
```

```
RAsym_2(counter,:) = -A.*sin(GammaRadA(counter).*x2);
```

```
RAsym_3_temp(counter,:) = ((-A.*sin(GammaRadA(counter).*(W_mmi/2)))./  
(cos(AlphaRadA(counter).*(W_mmi/2))-cot(AlphaRadA(counter).*(W_box2/2)).*  
sin(AlphaRadA(counter).*(W_mmi/2))))).*(cos(AlphaRadA(counter).*x3_2) -  
cot(AlphaRadA(counter).*(W_box2/2)).*sin(AlphaRadA(counter).*x3_2));
```

```
RAsym_temp(counter,:) = [RAsym_1_temp(counter,:) RAsym_2(counter,:) RAsym_3_temp(counter,:)];
```

```
% Inside actual simulation window
```

```
RAsym_1(counter,:) = ((A.*sin(GammaRadA(counter).*(W_mmi/2)))./  
(cos(AlphaRadA(counter).*(W_mmi/2))-cot(AlphaRadA(counter).*(W_box2/2)).*  
sin(AlphaRadA(counter).*(W_mmi/2))))).*(cos(AlphaRadA(counter).*x1) +  
cot(AlphaRadA(counter).*(W_box2/2)).*sin(AlphaRadA(counter).*x1));
```

```
RAsym_3(counter,:) = ((-A.*sin(GammaRadA(counter).*(W_mmi/2)))./  
(cos(AlphaRadA(counter).*(W_mmi/2))-cot(AlphaRadA(counter).*(W_box2/2)).*  
sin(AlphaRadA(counter).*(W_mmi/2))))).*(cos(AlphaRadA(counter).*x3) -  
cot(AlphaRadA(counter).*(W_box2/2)).*sin(AlphaRadA(counter).*x3));
```

```
RAsym(counter,:) = [RAsym_1(counter,:) RAsym_2(counter,:) RAsym_3(counter,:)];
```

```
% Normalize
```

```
RAsym(counter,:) = (1/sqrt(trapz(x_temp,RAsym_temp(counter,:).^2))).*  
RAsym(counter,:);
```



```

end

z = 0:dz:L; % Propagation-direction vector

zsteps = length(z); % Length of z-vector
xsteps = length(x); % Width of x-vector

%%%%% GUIDED Mode Coupling Coefficients
cS = zeros(length(GammaGuideS), length(z));
cA = zeros(length(GammaGuideA), length(z));
cRS = zeros(length(GammaRadS), length(z));
cRA = zeros(length(GammaRadA), length(z));

%%%%% Matrix corresponding to indices of refraction
index(:, :) = zeros(xsteps, zsteps);

for znum=1:zsteps
for xnum=1:xsteps
if( abs(x(xnum)) <= W_mmi/2)
index(xnum, znum) = n1; % In core
else
index(xnum, znum)=n2; % In cladding
end
end
end
end

```

```

Beta = sqrt(k1^2 - GammaSM^2);
Alpha = sqrt(Beta^2 - k2^2);

% Boundary condition continuity coefficient
B = E_amp.*cos(GammaSM.*W_sm/2)/exp(-Alpha.*(W_sm/2));

% Input electric field definition
for(counter = 1:length(x))
if(x(counter) < offset)
y(counter) = B.*exp(Alpha.*(x(counter) - (offset + W_sm/2)));
elseif(x(counter) > offset+W_sm)
y(counter) = B.*exp(-Alpha.*(x(counter) - (offset + W_sm/2)));
else
y(counter) = E_amp.*cos(GammaSM.*(x(counter) - (offset +
W_sm/2)));
end
end

E_sm = y; % Input electric field
Denom = trapz(x,E_sm.*conj(E_sm)); % Normalization Multiplier
I_sm = abs(E_sm).^2; % Input electric field intensity
P_sm = trapz(x,I_sm); % Input power

E_out = zeros(xsteps,zsteps); % Electric field after step
I_out = E_out;

```

%%%%%%%% Create matrix corresponding to patterned active regions%%%%%%%%

%%%% This divides the PARMS into 4 section with two twin gain regions

%%%% Region 1 & 2 are the same length as are region 3 & 4

%%% Gain for 4 sections and cladding

GdB1 = -5;

GdB2 = -5;

GdB3 = -20;

GdB4 = 10;

GdBclad = 0;

%%% Lengths of active regions

L1 = .8375e-3; % Length of regions 1 & 2

L2 = L - L1; % Length of regions 3 & 4

Gclad = 10^(GdBclad/10);

g0clad = log(Gclad)/z(length(z));

G1 = 10^(GdB1/10);

g01 = log(G1)/L1;

G2 = 10^(GdB2/10);

g02 = log(G2)/L1;

G3 = 10^(GdB3/10);

g03 = log(G3)/L2;

```

G4 = 10^(GdB4/10);
g04 = log(G4)/L2;

for znum=1:length(z)
if(z(znum) <= L1)
for xnum=1:xsteps
if( abs(x(xnum)) <= W_mmi/2)
if(x(xnum) >= 0)
% Gain 1
index(xnum,znum) = n1;
g0_vec(xnum,znum) = g01;
if(g0_vec(xnum,znum) >= 0)
% Saturation intensity for the section if biased to transparency
% or gain
Isat(xnum,znum) = 1;
else
% Saturation intensity if region is absorbing
Isat(xnum,znum) = .5789;
end
else
% Gain 2
index(xnum,znum) = n1;
g0_vec(xnum,znum) = g02;
if(g0_vec(xnum,znum) >= 0)
Isat(xnum,znum) = 1;
else

```

```

Isat(xnum,znum) = .5789;
end
end
else
%Cladding
index(xnum,znum)=n2;
g0_vec(xnum,znum) = g0clad;
Isat(xnum,znum) = 100;
end
end
else
for xnum=1:xsteps
if( abs(x(xnum)) <= W_mmi/2)
if(x(xnum) <= 0)
% Gain 4
index(xnum,znum) = n1;
g0_vec(xnum,znum) = g04;
if(g0_vec(xnum,znum) >= 0)
Isat(xnum,znum) = 1;
else
Isat(xnum,znum) = .5789;
end
elseif (x(xnum) <= W_mmi/2)
% Gain 3
index(xnum,znum) = n1;
g0_vec(xnum,znum) = g03;
if(g0_vec(xnum,znum) >= 0)

```

```

Isat(xnum,znum) = 1;
else
Isat(xnum,znum) = .5789;
end
else
% Cladding
index(xnum,znum) = n2;
g0_vec(xnum,znum) = g0clad;
Isat(xnum,znum) = 100;
end
else
% Cladding
index(xnum,znum)=n2;
g0_vec(xnum,znum) = g0clad;
Isat(xnum,znum) = 100;
end
end
end
end

E_sm_no_gain = E_sm;
L_sm = L_sm';
E_sm = exp(.5.*(g0_vec(:,1)./(1+(L_sm./Isat(:,1)))).*(1+j.*alpha).*dz).*
E_sm_no_gain';
E_sm = E_sm';

%%%%%% Determine coupling of input electric field into multimode

```

```

% Guided, symmetric
for counter = 1:length(GammaGuideS)
cS(counter,:) = trapz(x,E_sm.*conj(Sym(counter,:)))/Denom; %Overlap integral
E_out(:,1) = E_out(:,1) + (cS(counter,1).*Sym(counter,:))';
end

```

```

% Guided, asymmetric
for counter = 1:length(GammaGuideA)
cA(counter,:) = trapz(x,E_sm.*conj(Asym(counter,:)))/Denom;
E_out(:,1) = E_out(:,1) + (cA(counter,1).*Asym(counter,:))';
end

```

```

% Radiative, symmetric
for counter = 1:length(GammaRadS)
cRS(counter,:) = trapz(x,E_sm.*conj(RSym(counter,:)))/Denom;
E_out(:,1) = E_out(:,1) + (cRS(counter,1).*RSym(counter,:))';
end

```

```

% Radiative, asymmetric
for counter = 1:length(GammaRadA)
cRA(counter,:) = trapz(x,E_sm.*conj(RAsym(counter,:)))/Denom;
E_out(:,1) = E_out(:,1) + (cRA(counter,1).*RAsym(counter,:))';
end

```

```

E_out(:,1) = E_out(:,1).*Denom; % electric field shape after coupling into MMI
I_out(:,1) = E_out(:,1).*conj(E_out(:,1)); % Coupled intensity

```

```

P_out(1) = trapz(x,L_out(:,1)); % Coupled power

%%%%%%%%%%%%%%%%%%%%%%%%%%%%%%%%%%%%%%%%%%%%%%%%%%%%%%%%%%%%%%%%%%%%%%%% MPA with radiative modes and nonlinearities %%%%%%%%%

for countz = 2:length(z)

    %%% Guided, Symmetric %%%
    for counter = 1:length(GammaGuideS)
        E_out(:,countz) = E_out(:,countz) + (cS(counter,countz-1).*Sym(counter,:).*
        exp(j.*(BetaGuideS(1) - BetaGuideS(counter)).*z(countz)))';
    end

    %%% Guided, Asymmetric %%%
    for counter = 1:length(GammaGuideA)
        E_out(:,countz) = E_out(:,countz) + (cA(counter,countz-1).*Asym(counter,:).*
        exp(j.*(BetaGuideS(1) - BetaGuideA(counter)).*z(countz)))';
    end

    %%% Radiative, Symmetric %%%
    for counter = 1:length(GammaRadS)
        E_out(:,countz) = E_out(:,countz) + (cRS(counter,countz-1).*RSym(counter,:).*
        exp(j.*(BetaGuideS(1) - BetaRadS(counter)).*z(countz)))';
    end

    %%% Radiative, Asymmetric %%%
    for counter = 1:length(GammaRadA)
        E_out(:,countz) = E_out(:,countz) + (cRA(counter,countz-1).*

```



```

RAsym(counter,:).*exp(j.*(BetaGuideS(1) -
BetaRadA(counter)).*z(countz)))';
end

E_out(:,countz) = E_out(:,countz).*Denom; % Normalize
I_out(:,countz) = abs(E_out(:,countz)).^2; % Intensity

g = g0_vec(:,countz)./(1 + (I_out(:,countz)./Isat(:,countz))); % Gain vector at this
step
E_out_temp = exp(.5.*g.*(1+j.*alpha).*dz).*E_out(:,countz); % E-field after gain
I_out_temp = abs(E_out_temp).^2; % Intensity after gain
g = g0_vec(:,countz)./(1 + (I_out_temp./Isat(:,countz))); % Redetermine gain
E_out(:,countz) = exp(.5.*g.*(1+j.*alpha).*dz).*E_out(:,countz); % New e-field af-
ter gain
I_out(:,countz) = abs(E_out(:,countz)).^2; % Intensity

%%%%% Determine new coupling coefficients %%%%%

%%%%% Guided, Symmetric %%%%
for counter = 1:length(GammaGuideS)
cS(counter, countz) = (trapz(x,E_out(:,countz)).*conj(Sym(counter,:)).*
exp(j*(BetaGuideS(1)-BetaGuideS(counter)).*z(countz))))'./Denom;
end

%%%%% Guided, Asymmetric %%%%
for counter = 1:length(GammaGuideA)
cA(counter, countz) = (trapz(x,E_out(:,countz)).*conj(Asym(counter,:)).*

```

```
exp(j*(BetaGuideS(1)-BetaGuideA(counter)).*z(countz)))')')./Denom;
end
```

```
%%% Radiative, Symmetric %%%
```

```
for counter = 1:length(GammaRadS)
cRS(counter, countz) = (trapz(x,E_out(:,countz)).*conj(RSym(counter,:)).*
exp(j*(BetaGuideS(1)-BetaRadS(counter)).*z(countz)))')')./Denom;
end
```

```
%%% Radiative, Asymmetric %%%
```

```
for counter = 1:length(GammaRadA)
cRA(counter, countz) = (trapz(x,E_out(:,countz)).*conj(RAsym(counter,:)).*
exp(j*(BetaGuideS(1)-BetaRadA(counter)).*z(countz)))')')./Denom;
end
```

```
P_out(countz) = trapz(x,L_out(:,countz)); % Power after step
end
```

```
%%%%%%%%%%%%%%%%%%%%%%%%%%%%%%%%%%%%%%%%%%%%%%%%%%%%%%%%%
```

```
%%% Create input intensity matrix
```

```
L_in(:,1) = abs(E_sm).^2;
```

```
for count = 1:50
```

```
L_in(:,count+1) = L_in(:,count);
```

```
end
```

```

z_in = linspace(-.25*L,0,50); % Input z-vector

%%%% Plot figure and outline input waveguide and MMI
figure1 = figure;
axes1 = axes(...
'FontSize',14,...
'Layer','top',...
'Parent',figure1);
imagesc(z_in,x,I_in);
hold on;
imagesc(z,x,I_out);
hold off;
axis tight;

xlabel(axes1,'z(m)');
ylabel(axes1,'y(m)');

%%%%%%%%%%%%%%%%%%%%%%%%%%%%%%%%%%%%%%%%

%%%% Simulate dual output waveguide
[index3,E_sm_out2,zout] = DualGuides_lim(n1,n2,lambda,W_sm,abs(offset)-W_sm,
W_box/2,E_out(:,zsteps)',dx,15e-6,15e-6);

```

BIBLIOGRAPHY

- [1] National Research Council, *Harnessing light: optical science and engineering for the 21st century* (National Academy, Washington, D.C., 2000)
- [2] E. Davis, "Working fiber optics," *Security* **40**, 36-38 (2003).
- [3] J.H.R. Schrader, E.A.M. Klumperink, J.L. Visschers, and B. Nauta, "Data communications in read-out systems: how fast can we go over copper wires?," *Nucl. Instr. and Meth. A* **531**, 221-227 (2004).
- [4] J.D. Jackson, *Classical Electrodynamics (3rd)* (Wiley, New York, 1999).
- [5] C. Knöll, M. Gölles, Z. Bakonyi, G. Onishchukov, and F. Lederer, "Optimization of signal transmission by an in-line semiconductor optical amplifier-saturable absorber module," *Opt. Comm.* **187**, 141-153 (2001).
- [6] L.J. Christiansen, L. Xu, K. Yvind, F. Öhman, L. Oxenløwe, and J. Mørk, "2R regeneration in concatenated semiconductor optical amplifiers and electroabsorbers," in *Proceedings 30th ECOC*, Stockholm, Sweden, 2004.
- [7] J.D. Merlier, G. Morthier, S. Verstuyft, T. Van Caenegem, I. Moerman, P. Van Daele, and R. Baets, "Experimental demonstration of all-optical regeneration using an MMI-SOA," *IEEE Photon. Tech. Lett.* **14**, 660-662 (2002).
- [8] J.D. Merlier, G. Morthier, T. Van Caenegem, R. Baets, I. Moerman, and P. Van Daele, "Experimental demonstration of 15dB extinction ratio improvement in a new 2R optical regenerator using an MMI-SOA," in *Proceedings 27th ECOC*, Amsterdam, The Netherlands, 2001.
- [9] C. Davis, *Lasers and Electro-Optics: Fundamental and Engineering* (Cambridge University, Cambridge, 2000).

- [10] S. Ramo, J.R. Whinnery, and T. van Duzer, *Fields and Waves in Communication Electronics (3rd)* (Wiley-Interscience, New York, 1994).
- [11] G.B. Hocker and W.K. Burns, "Mode dispersion in diffused channel waveguides by the effective index method," *Appl. Opt.* **16**, 113-118 (1977).
- [12] K. Kawano and T. Kitoh, *Introduction to Optical Waveguide Analysis* (Wiley-Interscience, New York, 2001).
- [13] C.R. Pollock, *Fundamentals of Optoelectronics* (Irwin, Chicago, 1995).
- [14] M. Hammer, *1-D multilayer slab waveguide mode solver*. Retrieved July 15, 2005, from <http://wwwhome.math.utwente.nl/hammer/oms.html>
- [15] M. Hammer, *2-D multilayer slab waveguide mode solver*. Retrieved July 15, 2005, from <http://wwwhome.math.utwente.nl/hammer/eims.html>
- [16] K.F. Riley, M.P. Hobson, and S.J. Bence, *Mathematical methods for physics and engineering* (Cambridge University, Cambridge, 2003).
- [17] L.B. Soldano and E.C.M. Pennings, "Optical multi-mode interference devices based on self-imaging: principles and applications," *J. of Lightwave Tech.* **13**, 615-627 (1995).
- [18] R.M. Jenkins, R.W.J. Devereux, and J.M. Heaton, "Waveguide beam splitters and recombiners based on multimode propagation phenomena," *Opt. Lett.* **17**, 991-993 (1992).
- [19] M. Takenaka and Y. Nakano, "Multimode interference bistable laser diode," *IEEE Photo. Tech. Lett.* **15**, 1035-1037 (2003).
- [20] M. Takenaka and Y. Nakano, "Realization of all-optical flip-flop based on bistable laser diode with active multimode interference cavity," presented at Optical Fiber Communications Conference, 2004. (OFC 2004).

- [21] A.W. Snyder and J.D. Love, “Goos-Hänchen shift,” *Appl. Opt.* **15**, 236-238 (1976).
- [22] P.A. Besse, M. Bachmann, H. Melchior, L.B. Soldano, and M.K. Smit, “Optical bandwidth and fabrication tolerances of multimode interference couplers,” *J. of Lightwave Tech.* **12**, 1004-1009 (1994).
- [23] G. P. Agrawal and N.A. Olsson, “Self-phase modulation and spectral broadening of optical pulses in semiconductor laser amplifiers,” *IEEE J. of QE*, **25**, 2297-2306 (1989).
- [24] C.H. Henry, “Theory of the linewidth of semiconductor lasers,” *IEEE J. of QE* **QE-18**, 259-264 (1982).
- [25] M. Osiniński and J. Buus, “Linewidth broadening factor in semiconductor lasers – An overview,” *IEEE. J. of QE* **QE-23**, 9-29 (1987).
- [26] L. Occhi, L. Schares, and G. Guekos, “Phase modeling based on the α -factor in bulk semiconductor optical amplifiers,” *IEEE J. of S.T. in QE* **9**, 788-797 (2003).
- [27] R. Scarmozzino, A. Gopinath, R. Pregla, and S. Helfert, “Numerical techniques for modeling guided-wave photonic devices,” *IEEE J. of S.T. in QE* **6**, 150-162 (2000).
- [28] Durrant, D.R., *Numerical Methods for Wave Equations in Geophysical Fluid Dynamics* (Springer-Verlag, New York, 1999).
- [29] P. Kaczmarek and P.E. Lagasse, “Bidirectional beam propagation method,” *Electron. Lett.* **24**, 675-676 (1988).

- [30] R. Hongling, R. Scarmozzino, and R.M. Osgood, Jr., “A bidirectional beam propagation method for multiple dielectric interfaces,” *IEEE Photon. Tech. Lett* **11**, 830-832 (1999).
- [31] F. Wijnands, H.J.W.M. Hoekstra, G.J.M. Krijnen, and R.M. de Ridder, “Numerical solution method of nonlinear guided modes with a finite difference complex axis beam propagation method,” *IEEE J. of QE* **31**, 782-790 (1995).
- [32] H.M. Masoudi and J.M. Arnold, “Modeling second-order nonlinear effects in optical waveguides using a parallel-processing beam propagation method,” *IEEE J. of Q.E.* **31**, 2107-2113 (1995).
- [33] G.R. Hadley, “Multistep method for wide-angle beam propagation,” *Opt. Lett.* **24**, 1743-1745 (1992).
- [34] B.A.M. Rahman, and J.B. Davies, “Finite-element analysis of optical and microwave waveguide problems,” *IEEE Trans. on. Microwave Theory and Techniques* **MTT-32**, 20-28 (1984).
- [35] K. Kawano, T. Kitoh, M. Kohtoku, T. Ito, “Bidirectional finite-element method-of-line beam propagation method (FE-MoL-BPM) for analyzing optical waveguides with discontinuities,” *IEEE Photon. Tech. Lett.* **10**, 244-245 (1998).
- [36] M. Zoboli and S. Seileri, “Analysis of nonlinear slab waveguides through FEM formulations,”
- [37] K. Hayata, M. Koshiba, and M. Suzuki, “Finite-element solution of arbitrarily nonlinear, graded-index slab waveguides,” *Electron. Lett.* **23**, 429-431 (1987).

- [38] S.D. Gedney and U. Navsariwala, "An unconditionally stable finite element time-domain solution of the vector wave equation," *IEEE Microwave and Guided Wave Lett.* **5**, 332-334 (1995).
- [39] P. Gerard, P. Benech, D. Khalil, R. Rimet, and S. Tedjini, "Towards a full vectorial and modal technique for the analysis of integrated optics structures: the radiation spectrum method (RSM)," *Opt. Comm.* **140**, 128-145 (1997).
- [40] N.F. Dasyras, I.G. Tigelis, A.D. Tsigopoulos, and A.B. Manenkov, "Calculation of radiation modes by the Lanczos-Fourier expansion," *JOSA A* **21**, 1740-1749 (2004).
- [41] J.C. Cambell and T. Li, "Electro-optic multimode waveguide modulator or switch," *J. Appl. Phys* **50**, 6149-6154 (1979).
- [42] P.V. Petruzzi, "Optical pattern recognition using a segmented semiconductor optical amplifier," in Ph.D. dissertation, University of Maryland, College Park, 2003.